J. Mech. Phys. Solids 168 (2022) 105055

Contents lists available at ScienceDirect

Journal of the Mechanics and Physics of Solids

journal homepage: www.elsevier.com/locate/jmps

Surface pattern formation induced by oscillatory loading of frontally polymerized gels

Aditya Kumar [a,c], Leon M. Dean [b,c], Mostafa Yourdkhani [d], Allen Guo [b,c], Cole BenVau [b,c], Nancy R. Sottos [b,c], Philippe H. Geubelle [a,c,*]

[a] Department of Aerospace Engineering, University of Illinois, Urbana–Champaign, IL 61801, USA
[b] Department of Materials Science and Engineering, University of Illinois, Urbana–Champaign, IL 61801, USA
[c] Beckman Institute for Advanced Science and Technology, University of Illinois, Urbana–Champaign, IL 61801, USA
[d] Department of Mechanical Engineering, Colorado State University, CO 80523, USA

ARTICLE INFO

Keywords:
Frontal polymerization
Thermo-chemo-mechanical coupling
Surface pattern formation
Reaction–diffusion
Nonlinear mechanics

ABSTRACT

Frontal polymerization (FP) is a rapid, energy-efficient technique for the manufacturing of polymeric materials and composites. It has also emerged as a way to rapidly alter the shape of partially cured polymeric materials through mechanical deformation. The first objective of this paper is to introduce a coupled thermo-chemo-mechanical theory capable of describing within the framework of nonlinear kinematics the evolution of deformation and temperature fields during frontal polymerization of gels. At the heart of the proposed theory is the introduction of eigenstrains corresponding to the phase transformation prompted by the frontal curing process. Another objective is to introduce a novel bio-inspired oscillatory loading-induced patterning technique in which we form thermoset polymeric materials with periodic surface topography patterns by applying oscillatory uniaxial loads to partially cured gels during FP. After a detailed presentation of the experimental methodology, the theoretical predictions are compared with experimental results.

1. Introduction

Frontal polymerization (FP) involves a self-propagating exothermic reaction front that converts a liquid monomer or partially cured gel to a fully cured polymer (Chechilo et al., 1972; Khanukaev et al., 1974; Chechilo and Enikolopyan, 1974; Davtyan et al., 1984; Pojman, 1991; Pojman et al., 1995). The reaction front is initiated ordinarily by a local thermal stimulus applied to a mixture of monomer and catalyst. The heat generated by the exothermic reaction in turn advances the propagating front by thermal diffusion, resulting in a self-sustained process as shown in Fig. 1(a).

FP provides a rapid, energy-efficient, and scalable method for manufacturing polymeric materials and composites (Robertson et al., 2017, 2018; Ivanoff et al., 2020). Moreover, FP of partially cured gels has enabled simultaneous free-form 3D printing and curing (Aw, 2019; Aw et al., 2022) (Fig. 1(b)), as well as a way to alter the shape of a material by mechanical deformation or embossing (Fig. 1(c)). In this work, we focus our attention on the latter application although the proposed theoretical framework is also applicable to FP-based printing.

Mathematical modeling of FP in the literature has so far focused mostly on the thermo-chemical process in polymers and fiber-reinforced polymer composites; see Goli et al. (2018) and discussion therein. The emphasis of the modeling work has been to estimate

* Corresponding author at: Department of Aerospace Engineering, University of Illinois, Urbana–Champaign, IL 61801, USA.
E-mail addresses: akumar51@illinois.edu (A. Kumar), lmdean2@illinois.edu (L.M. Dean), mostafa.yourdkhani@colostate.edu (M. Yourdkhani), allenxg2@illinois.edu (A. Guo), benvau2@illinois.edu (C. BenVau), n-sottos@illinois.edu (N.R. Sottos), geubelle@illinois.edu (P.H. Geubelle).

https://doi.org/10.1016/j.jmps.2022.105055
Received 21 February 2022; Received in revised form 6 June 2022; Accepted 29 August 2022
Available online 5 September 2022

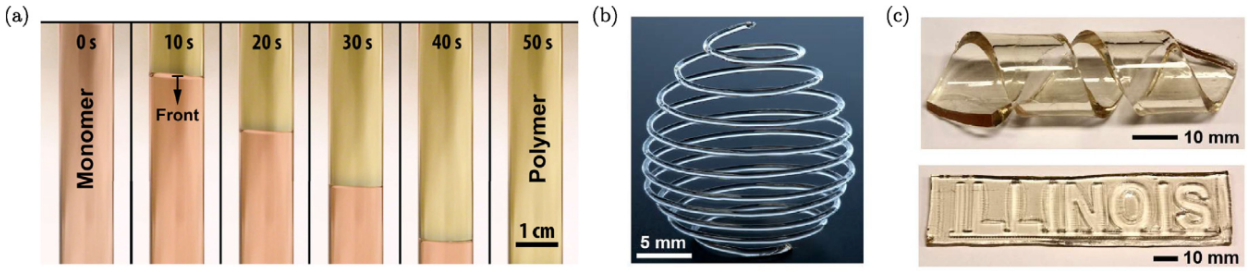

Fig. 1. (a) Images showing propagation of a polymerization front through a test tube. Adapted from Robertson et al. (2017). Copyright 2017 American Chemical Society. (b) Ball helix structure produced via freeform 3D printing and FP of partially cured DCPD. (c) Macropatterned structures produced via deformation (top) or embossing (bottom) of a DCPD gel prior to FP. (b) and (c) adpated from Robertson et al. (2018). Copyright 2018 Springer Nature.

key front characteristics like maximum temperature and velocity (Goldfeder et al., 1997; Frulloni et al., 2005; Goli et al., 2018; Vyas et al., 2019; Kumar et al., 2021) and stability (Solovyov et al., 1997; Goli et al., 2020). The study of front instabilities has also inspired the investigation of fluid convection effects in bounded domains during FP (Pojman et al., 1992; Volpert et al., 1996; Garbey et al., 1996; Bowden et al., 1997). As an initial step towards constructing a general theory, the first objective of this work is to construct a macroscopic solid-to-solid phase transformation theory capable of describing and predicting the thermo-chemo-mechanical processes taking place during FP of gels. The theory needs to be situated within large deformation mechanics due to the very compliant (and nearly incompressible) mechanical behavior of gel. The central idea in this work is to introduce eigenstrains corresponding to the phase transformation brought upon by the polymerization reaction. This phase transformation causes the material stiffness to typically increase by three to four orders of magnitude, essentially freezing the material in its deformed configuration. We also provide the finite-element based numerical implementation for the theory.

Theoretical and computational work in the area of thermo-chemo-mechanical modeling has attracted a lot of attention in the past few decades, especially in applications related to energy conversion and storage devices such as fuel cells and batteries (Haftbaradaran et al., 2011; Gao et al., 2015). Most of the modeling work has been conducted in the realm of small deformations. However, some recent work has incorporated nonlinear kinematic effects (Cui et al., 2012; Anand, 2012). A notable contribution in this line of work is that by Anguiano et al. (2020), Anguiano and Masud (2021) who presented a chemo-mechanical formulation and its variational multiscale numerical implementation to study large chemically induced swelling deformations in problems like silicon oxidation and lithiation. Related modeling work can be found in the context of chemical reaction-caused expansion in concrete (Ulm et al., 2000), hydrogels (Cai and Suo, 2011) and other materials. Furthermore, significant attention has also been given to mechanical modeling of growth and aging processes (Epstein and Maugin, 2000; Epstein, 2015; Sozio and Yavari, 2019; Javadi et al., 2020) with application to materials like biological tissues (Ambrosi et al., 2011; Kuhl, 2014) and Li-ion batteries (Rejovitzky et al., 2015; Di Leo et al., 2015). These processes involve the generation of eigenstrains and residual stresses primarily due to mass variation, rather than purely due to a reaction–diffusion processes in a fixed domain like in the current work. A key challenge of multi-physics modeling is often associated with a lack of comprehensive experimental data. The work presented hereafter, however, builds on the extensive prior characterization of mechanical, thermal, and chemical behavior during FP (Yourdkhani et al., 2019; Koohbor et al., 2022).

The second main objective of this work is to describe the development of a novel, bio-inspired patterning technique in which thermosets are formed with periodic surface topography patterns by applying oscillatory loading to dicyclopentadiene (DCPD) gels during FP. In contrast to prior demonstrations of surface patterning using photo-FP (Ma et al., 2013), this technique enables patterning on multiple surfaces of a single sample, with surface composition and properties identical to the bulk material. We also study this technique analytically and numerically with the proposed theory and conduct detailed comparisons with experimental observations.

The inspiration for oscillatory loading-induced patterning comes from nature. There is strong evidence that mechanical forces in the basal layer of the fetal epidermis create buckling instabilities that lead to the formation of fingerprints (Kucken and Newell, 2005). Mechanical forces also cause cortical folding, a process critical to human brain development, although the relative contributions of hypothesized mechanisms are still in dispute (Van Essen, 1997; Bayly et al., 2014). Beyond these surface patterns, the morphology and properties of bulk biological materials can also be modulated by mechanical stress. For example, bone remodeling is a cellular process in which the bone structure is adapted to optimize for the mechanical stresses it experience (Robling et al., 2006; Warden et al., 2014; Weinkamer et al., 2019). This short list of biological processes for mechanically-induced pattern formation offers tremendous inspiration for the manufacturing of synthetic materials. However, these biological processes are much too complex for direct imitation and also operate on a lengthy timescale impractical for synthetic manufacturing. In contrast, the FP-based patterning technique presented here is simple and rapid.

The organization of the paper is as follows. In Section 2, we construct the theory for thermo-chemo-mechanical process during frontal polymerization. We do so by first introducing the eigenstrains corresponding to thermal expansion and phase transformation brought on by chemical curing. Then we describe the kinematics, balance relations, and constitutive relations for this process to formulate the initial–boundary-value problem with emphasis on capturing the changes in the natural stress-free configuration of the material due to the freezing of deformations during FP curing. The theory amounts to solving a system of three coupled, nonlinear

partial differential equations (PDEs) for the deformation field χ, temperature field T, and an internal variable α that represents the degree of cure. Section 3 introduces a finite-element scheme to solve these equations numerically. The weak form of the PDEs is time-discretized with a first-order finite-difference scheme, whereas we employ for space discretization a non-conforming low-order finite element that has been recently shown (Kumar et al., 2018) to work efficiently in large deformations with nearly incompressible soft materials. The accuracy of the scheme is verified by solving an idealized 1-D problem for which we generate an analytical solution. In Section 4, we illustrate the workings of the theory and explore its descriptive capabilities by carrying out 2-D simulations on a DCPD specimens subjected to static and oscillatory tension and different thermal initial conditions. Then, in Section 5, we present the experimental methodology for the bioinspired oscillatory loading-induced FP-based patterning technique. Finally, we compare the theoretical predictions with experimental results.

2. Coupled thermo-chemo-mechanical formulation under finite deformations

2.1. Kinematics

Consider a solid that occupies in its initial reference configuration (at time $t = 0$) a bounded domain $\Omega_0 \subset \mathbb{R}^N$, with boundary $\partial\Omega_0$ and unit outward normal $\mathbf{N}$. The density of the solid is denoted as ρ_0. We identify material points by their initial position vector $\mathbf{X} \in \Omega_0$. The initial temperature of the solid is denoted by $T_0(\mathbf{X})$. At a later time $t \in (0, t_1]$, due to externally applied mechanical and thermal stimuli to be described below, the position vector $\mathbf{X}$ of a material point moves to a new position specified by

$$\mathbf{x} = \chi(\mathbf{X}, t),$$

where χ is a mapping from Ω_0 to the current configuration $\Omega(t)$, also contained in $\mathbb{R}^N$. The temperature field in the current configuration is denoted by $\hat{T}(\mathbf{x}, t) \in \mathbb{R}^0$. The density of the solid in current configuration is $\rho(\mathbf{x}, t)$. We consider only invertible deformations and write the deformation gradient and particle velocity fields at $\mathbf{X}$ and t as

$$\mathbf{F}(\mathbf{X}, t) = \text{Grad}\, \chi(\mathbf{X}, t) \qquad \text{and} \qquad \dot{\chi}(\mathbf{X}, t) = \frac{\partial \chi}{\partial t}(\mathbf{X}, t). \tag{1}$$

Furthermore, the solid comprises of different phases in the current configuration, which we define using an internal variable (or order parameter)

$$\alpha = \hat{\alpha}(\mathbf{x}, t).$$

The internal variable $\alpha \in \mathbb{R}^0$, referred to hereafter as the degree of cure, takes a value between 0 and 1. Values $\alpha = 0$ and $\alpha = 1$ respectively denote the uncured and fully cured states of the polymer, and the transition from a phase with lower value of α to one with higher value is considered irreversible. Keeping in mind the problems of interest where the partially cured polymer is in a solid gel state, the initial degree of cure in the reference configuration is set to $\hat{\alpha}(\mathbf{x}, 0) = \alpha_0$. We further define the direction of front propagation at $\mathbf{X}$ as $\mathbf{m}(\mathbf{X}, t)$ defined by $\nabla_{\mathbf{X}} \hat{\alpha} \cdot \mathbf{m} < 0$.

It is well known that thermal expansion/contraction can result in an updated natural (stress-free) configuration with residual deformation relative to initial configuration Ω_0. We represent the deformation gradient due to thermal expansion/contraction by a second-order tensor $\mathbf{F}^\theta$. In a similar vein, the curing of the material has also been observed experimentally to result in a new natural configuration due to irreversible freezing of deformation at material points $\mathbf{X}$ at the passage of the polymerization front as the degree of cure increases from its initial value to the fully cured state corresponding to $\alpha = 1$. We represent the deformation gradient due to such process by another second-order tensor $\mathbf{F}^r$. Then, we define a total deformation gradient tensor as a multiplicative decomposition

$$\tilde{\mathbf{F}} = \mathbf{F}\mathbf{F}^{\theta^{-1}}\mathbf{F}^{r^{-1}}. \tag{2}$$

Such a decomposition, commonly adopted in constitutive modeling of plasticity and viscoelasticity, reduces to the following additive decomposition in the limit of small deformations:

$$\tilde{\boldsymbol{\varepsilon}} = \boldsymbol{\varepsilon} - \boldsymbol{\varepsilon}^\theta - \boldsymbol{\varepsilon}^r, \tag{3}$$

where $\boldsymbol{\varepsilon} = 1/2\,(\mathbf{F} + \mathbf{F}^T - 2\mathbf{I})$, $\boldsymbol{\varepsilon}^\theta$ is the classical eigenstrain due to thermal expansion and $\boldsymbol{\varepsilon}^r$ is similarly an eigenstrain associated with curing. We will refer to $\mathbf{F}^\theta$ and $\mathbf{F}^r$ as eigenstrains as well from here on. It should be noted that (2) is a constitutive choice used to simplify the coupling between the three fields.

Fig. 2 shows a schematic of the material in its initial state Ω_0 at $t = 0$ and in the current state $\Omega(t)$ at a later time, illustrating the changes in deformation, temperature, and degree of cure fields. It also illustrates the two intermediate configurations $\Omega_\theta(t)$ and $\Omega_r(t)$ that appear as a result of the assumed multiplicative decomposition (2).

2.2. Balance relations

The balance of linear momentum in the absence of inertia is described by

$$\text{Div}\, \mathbf{S}(\mathbf{X}, t) + \mathbf{B}(\mathbf{X}, t) = 0, \quad (\mathbf{X}, t) \in \Omega_0 \times [0, t_1] \tag{4}$$

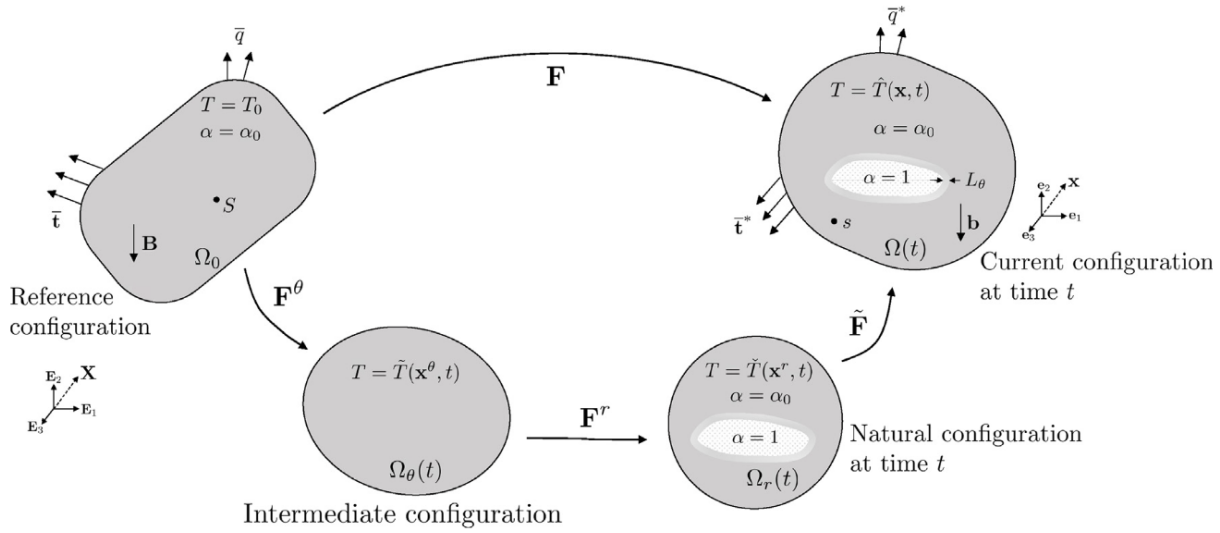

Fig. 2. Schematic of the polymer in its initial stress-free configuration at time $t = 0$ with initial temperature T_0 and initial degree of cure α_0, and at a later time $t > 0$ defined by the deformation mapping $\chi(\mathbf{X}, t)$ (and its gradient $\mathbf{F}(\mathbf{X}, t)$) and temperature field $\hat{T}(\mathbf{x}, t)$. The schematic also shows the evolution of the degree of cure α in some regions of the polymer from α_0 to 1 representing the curing of the polymer. The $\alpha = \alpha_0$ and $\alpha = 1$ regions are separated by the polymerization front, i.e., a thin reaction zone whose width L_θ is governed by reaction kinetics. Furthermore, the intermediate configurations $\Omega_\theta(t)$ and $\Omega_r(t)$, with coordinate vectors $\mathbf{x}^\theta$ and $\mathbf{x}^r$ respectively, prompted by the multiplicative decomposition (2) are shown. The second intermediate configuration Ω_r also represents the new natural configuration at time t.

where $\mathbf{S}$ represents the first Piola–Kirchhoff stress tensor and $\mathbf{B}$ refers to the volumetric body force at each material point $\mathbf{X} \in \Omega_0$. For clarity, Div[·] refers to the divergence operator with respect to the material coordinate $\mathbf{X}$.

From the balance of energy, the transient heat equation describing the evolution of the thermal state in the solid in its current configuration $\Omega(\mathbf{x}, t)$ follows as

$$\rho C_p \frac{\partial \hat{T}}{\partial t}(\mathbf{x}, t) = -\text{div}\, \mathbf{q}(\mathbf{x}, t) + s(\mathbf{x}, t) + \rho r \left(\mathbf{F}, \hat{T}, \frac{\partial \hat{T}}{\partial t} \right), \quad (\mathbf{x}, t) \in \Omega \times [0, t_1] \tag{5}$$

where $\mathbf{q}$ represents the heat flux vector, s denotes the volumetric heat source term associated with the exothermic polymerization for the problem of interest, and C_p is the specific heat capacity of the solid assumed hereafter to be independent of α. div[·] refers to the divergence operator with respect to the spatial coordinate $\mathbf{x}$. Moreover, the term r captures the heating effect due to deformation. In the problems of interest in this work, this heating effect is expected to be negligible compared to the heat released from the exothermic chemical reaction. Hence, we will neglect this term from here onwards. Through a change of variables and using conservation of mass relation $\rho = (\det \mathbf{F})^{-1} \rho_0$, the balance of energy can be rewritten in terms of the reference coordinate as

$$\rho_0 C_p \frac{\partial T}{\partial t}(\mathbf{X}, t) = -\text{Div}\,(\mathbf{Q}) + S(\mathbf{X}, t), \quad (\mathbf{X}, t) \in \Omega_0 \times [0, t_1] \tag{6}$$

where $T(\mathbf{X}, t) = \hat{T}(\chi(\mathbf{X}, t), t)$, $\mathbf{Q} = J\mathbf{F}^{-1}\mathbf{q}$, and $J = \det \mathbf{F}$. The thermo-mechanical coupling is readily apparent from this relation.

The rate kinetics for the degree of cure α is assumed to be described by the relation (Goli et al., 2018)

$$\frac{\partial \alpha}{\partial t}(\mathbf{X}, t) = h(T, \alpha), \quad (\mathbf{X}, t) \in \Omega_0 \times [0, t_1]. \tag{7}$$

where $\alpha(\mathbf{X}, t) = \hat{\alpha}(\chi(\mathbf{X}, t), t)$ and $h(T, \alpha) \geq 0$. We assume here that the reaction kinetics remain unaffected by mechanical deformation, an assumption supported by experimental observations.

2.3. Constitutive relations

Assuming that the polymer of interest is isotropic, we define the eigenstrain $\mathbf{F}^\theta$ as

$$\mathbf{F}^\theta(\mathbf{X}, t) = g(T(\mathbf{X}, t), \alpha(\mathbf{X}, t))\, \mathbf{I}, \quad \text{with} \quad g(T, \alpha) = 1 + \zeta(T, \alpha)(T - T_0) \tag{8}$$

where $\zeta(T, \alpha)$ is the thermal expansion coefficient for the material. The dependence of the thermal expansion coefficient on the local temperature and degree-of-cure values is complex and likely depends on the temperature relative to the local glass transition temperature, which is itself a function of the local degree of cure. In the absence of accurate measurements for DCPD, we adopt hereafter a constant value $\zeta = 10^{-4}$ K^{-1}, which corresponds to the value for fully polymerized DCPD (Koohbor et al., 2022) .

The second-order tensor $\mathbf{F}^r(\mathbf{X}, t)$ is equal to identity tensor $\mathbf{I}$ if the reaction front has not arrived at the material point $\mathbf{X}$ at time t. The time of arrival of a sharp polymerization front is defined as $t^*(\mathbf{X})$ when the material state switches from $\alpha = \alpha_0$ to $\alpha = 1$. At $t = t^*(\mathbf{X})$, the natural state of material point $\mathbf{X}$ irreversibly updates to the deformed state of the material infinitesimally ahead of

the front representing a freezing of deformations due to chemical reaction. This update of the natural state is represented through a change in the value of tensor $\mathbf{F}^r(\mathbf{X},t)$. Hence, we define

$$\mathbf{F}^r(\mathbf{X},t) = \begin{cases} \mathbf{F}(\mathbf{X}^+,t^*(\mathbf{X}))\,\mathbf{F}^{\theta^{-1}}(\mathbf{X}^+,t^*(\mathbf{X})), & \text{if} \quad t \geq t^*(\mathbf{X}) \\ \mathbf{I}, & \text{otherwise} \end{cases} \tag{9}$$

where $\mathbf{X}^+ = \mathbf{X} + \epsilon\,\mathbf{m}$. Here, ϵ is an infinitesimal constant and $\mathbf{m}(\mathbf{X},t^*)$ was defined earlier as $\nabla_{\mathbf{X}}\hat{\alpha}\cdot\mathbf{m} < 0$. In reality, since the polymerization front has a small but finite thickness L_θ (Goli et al., 2018) as schematically shown in Fig. 2, the material can exist in a phase for which $\alpha_0 < \alpha < 1$. Therefore, we regularize $\mathbf{F}^r$ as

$$\mathbf{F}^r(\mathbf{X},t) = \begin{cases} \left(\mathbf{I} + \int_0^1 f(\alpha;C,\alpha^E-\alpha^h)\,(\mathbf{F}-\mathbf{I})\,d\alpha\right)\left(\mathbf{I} + \int_0^1 f(\alpha;C,\alpha^E-\alpha^h)\,\zeta(T-T_0)\,d\alpha\,\mathbf{I}\right)^{-1}, & \text{if } t \geq t^*(\mathbf{X}) \\ \mathbf{I}, & \text{otherwise} \end{cases} \tag{10}$$

where $t^*(\mathbf{X})$ is now defined such that $\alpha(\mathbf{X},t^*) = \alpha^E$ and infinitesimal constant ϵ is defined such that $\alpha(\mathbf{X}+\epsilon\,\mathbf{m},t^*) = \alpha^E - \alpha^h$. The function f is a scalar function of α and two positive constants $C, \alpha^E - \alpha^h$ that satisfy

$$\lim_{C\to\infty} f(\alpha;C,\alpha^E-\alpha^h) = \delta[\alpha - \alpha^E + \alpha^h], \tag{11}$$

with $\delta[\cdot]$ denoting the Dirac delta function. Clearly, for a large value of the constant C, the regularized form of $\mathbf{F}^r(\mathbf{X},t)$(10) reduces to (9). We specifically choose

$$f(\alpha) = \frac{C\,\exp(C(\alpha-\alpha^E+\alpha^h))}{(1+\exp(C(\alpha-\alpha^E+\alpha^h)))^2}. \tag{12}$$

This choice for the function f and the value of the constants C, α^E, and α^h are motivated by the evolution of elastic modulus with degree of cure specified below in (16). Having defined $\mathbf{F}^\theta$ and $\mathbf{F}^r$, we are now in position to prescribe the stress-deformation response, the flux-temperature response (Fourier's law), and the cure-kinetics relation.

Stress-deformation response. The nonlinear elastic behavior of the material is taken to be characterized by a free-energy function

$$\psi = \psi(\tilde{\mathbf{F}}),$$

which satisfies the requirement of material frame indifference[1] $\psi(\tilde{\mathbf{F}}) = \psi(\mathbf{Q}\tilde{\mathbf{F}})$ for all $Q \in \mathrm{Orth}^+$. The first Piola–Kirchhoff stress tensor $\mathbf{S}$ is defined as

$$\mathbf{S}(\mathbf{X},t) = \frac{\partial\psi}{\partial\mathbf{F}}(\tilde{\mathbf{F}}) = \frac{\partial\psi}{\partial\tilde{\mathbf{F}}}(\tilde{\mathbf{F}})\,\mathbf{F}^{\theta^{-1}}\,\mathbf{F}^{r^{-1}}. \tag{13}$$

A choice for free-energy function ψ to be adopted in the numerical simulations below is the compressible Neo-Hookean function

$$\psi(\tilde{\mathbf{F}},\alpha) = \frac{\mu(\alpha)}{2}\,(\tilde{I}_1 - 3) - \mu(\alpha)\,\ln(\tilde{J}) - \frac{\lambda(\alpha)}{2}\,(\tilde{J}-1)^2, \tag{14}$$

where $\tilde{I}_1 = \mathrm{tr}(\tilde{\mathbf{F}}^T\tilde{\mathbf{F}})$ and $\tilde{J} = \det(\tilde{\mathbf{F}})$. As is well known, the Neo-Hookean model is suitable for representing nonlinear elastic behavior under small to moderate deformations. For large deformations, other non-Gaussian models need to be adopted (Gent, 1996; Lopez-Pamies, 2010). The positive scalar material property functions $\mu(\alpha)$ and $\lambda(\alpha)$ represent the two Lamé constants for the polymer in different phases as a function of degree of cure α. For an isotropic material, the two material properties can be equivalently defined in terms of the Young's modulus and the Poisson's ratio as

$$\mu(\alpha) = \frac{E(\alpha)}{2(1+\nu(\alpha))}, \quad \lambda(\alpha) = \frac{E(\alpha)\nu(\alpha)}{(1+\nu(\alpha))(1-2\nu(\alpha))}. \tag{15}$$

When $\alpha = \alpha_0$, $E(\alpha) = E_1$ and $\nu(\alpha) = \nu_1$, where E_1 and ν_1 are the Young's modulus and Poisson's ratio of the soft partially cured polymer or gel. Similarly, when $\alpha = 1$, $E(\alpha) = E_2$ and $\nu(\alpha) = \nu_2$, where E_2 and ν_2 are the Young's modulus and Poisson's ratio of the fully cured (much stiffer) polymer. The values of $E(\alpha)$ and $\nu(\alpha)$ with $\alpha \geq 0.28$ were measured experimentally for DCPD by Koohbor et al. (2022) and Yourdkhani et al. (2019) as shown in Fig. 3 along with the best functional fit for the data described as[2]

$$E(\alpha) = E_2 + \frac{E_1 - E_2}{1+\exp(C(\alpha-\alpha^E))}, \quad \nu(\alpha) = \nu_2 + \frac{\nu_1 - \nu_2}{1+\exp(D(\alpha-\alpha^\nu))}. \tag{16}$$

The values of the fitting constants C, α^E, D, and α^ν in (16) are listed in Table 1 along with the values for E_1, ν_1, E_2, and ν_2. The choice for function $f(\alpha;k,\alpha^E-\alpha^h)$ in (12) is based on the above expression for $E(\alpha)$. Specifically, we adopt

$$f(\alpha) = \frac{d}{d\alpha}\left(\frac{E(\alpha+\alpha^h)-E_2}{E_1-E_2}\right) = \frac{C\,\exp(C(\alpha+\alpha^h-\alpha^E))}{(1+\exp(C(\alpha+\alpha^h-\alpha^E)))^2}, \tag{17}$$

where α^h is chosen as 0.39 such that $E(\alpha^E-\alpha^h) \approx 3E_1$. A verification study presented in Section 3.3 shows that this choice for the value of α^h is satisfactory for the accurate computation of the eigenstrain $\mathbf{F}^r$.

[1] The objectivity of free-energy function ensures the rotational balance $\mathbf{S}\mathbf{F}^T = \mathbf{F}\mathbf{S}^T$.

[2] The strong ellipticity of the free-energy function (14) is trivially satisfied with the choice for elastic property functions.

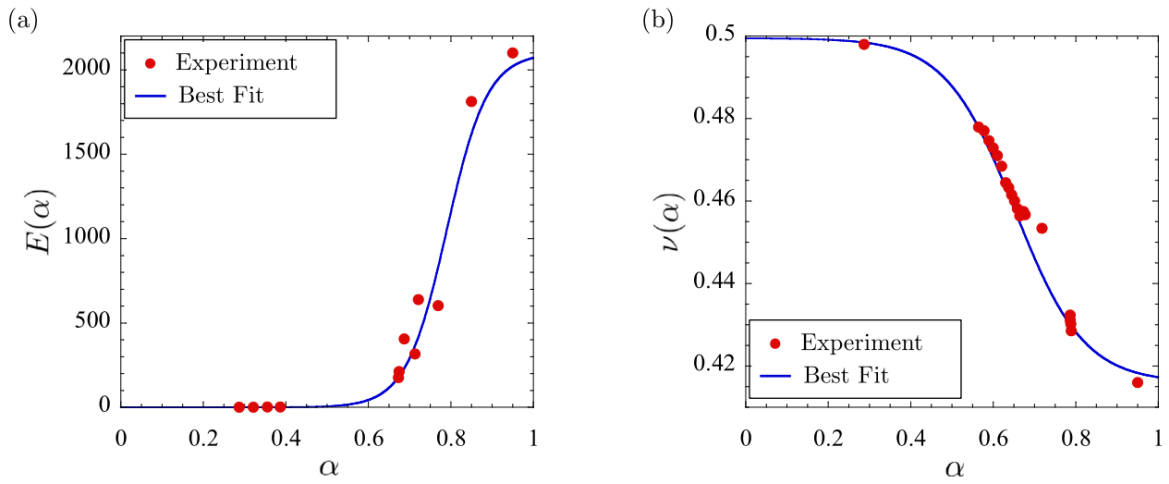

Fig. 3. Elastic properties of dicyclopentadiene (DCPD) measured experimentally by Koohbor et al. (2022) for various values of degree of cure α shown along with the best functional fit (16). (a) Young's modulus $E(\alpha)$, and (b) Poisson's ratio $\nu(\alpha)$.
Source: Figure adapted from Koohbor et al. (2022).

Table 1
Elastic material parameters for dicyclopentadiene (DCPD).

$E_1 = 0.29$ MPa	$E_2 = 2100$ MPa	$C = 20.30$	$\alpha_E = 0.79$
$\nu_1 = 0.4995$	$\nu_2 = 0.416$	$D = 11.92$	$\alpha_\nu = 0.65$

Remark 1. The dependence of the elastic properties of DCPD on the degree of cure suggests the following two observations. Firstly, the Young's modulus E of DCPD increases by around four orders of magnitude from its partially-cured state of $\alpha = 0.28$ to the fully cured state. We also note that the definition of $\mathbf{F}^r$ is independent of the ratio E_2/E_1. Secondly, DCPD is nearly incompressible in its initial cure state. This near incompressibility requires the use of special finite element to numerically solve the initial–boundary-value problem as discussed in the next section. Moreover, we note that, in this work, the elastic properties are assumed to be a function of the degree of cure α only and not a direct function of temperature T or time.

Remark 2. In its partially cured gel state for $\alpha \geq 0.1$, the polymer has been observed to behave as a visco-elastic solid. Yet, as this paper presents the first effort to study the thermo-chemo-mechanical coupling in frontal polymerization, we idealize the partially cured polymer as an elastic solid. This assumption proves to be adequate to describe the experiments of interest in Section 5. In its current form, the model does not account for chemical shrinkage either, which could be incorporated in the proposed framework as an additional eigenstrain.

Fourier's law. The Fourier's law for heat conduction is defined as

$$\mathbf{q} = -\kappa \frac{\partial T}{\partial \mathbf{x}}, \tag{18}$$

where κ is the thermal conductivity of the isotropic resin, which is assumed to be constant. Through a change of coordinate, the Fourier's law can be written with respect to the reference configuration Ω_0 as

$$\mathbf{Q} = \kappa\, J\, \mathbf{F}^{-1}\mathbf{F}^{-T} \frac{\partial T}{\partial \mathbf{X}}, \tag{19}$$

where we recall that $J = \det \mathbf{F}$.

Cure kinetics relation. To describe the kinetics of the polymerization reaction of DCPD in (7), we adopt the following separable form with the temperature dependence captured by an Arrhenius law and the degree-of-cure dependence given by the modified Prout–Tompkins model:

$$h(T,\alpha) = A_a \exp\left(\frac{-E_a}{RT}\right) (1-\alpha)^n \alpha^m \frac{1}{1+\exp(c_d(\alpha-\alpha_d))}. \tag{20}$$

Here, A_a (in 1/s) is the time constant, E_a (in J/mol) is the activation energy, R (=8.314 J/(mol K)) is the universal gas constant, n and m are two exponents that define the order of reaction in Prout–Tompkins model while c_d and α_d are two constants that describe the diffusion-controlled reaction kinetics at high values of α (Yang and Lee, 2014). The thermal and cure kinetics parameters that appear in (19)–(20) are listed in Table 2.

Table 2
Thermal and cure kinetic material parameters for dicyclopentadiene (DCPD) (Vyas et al., 2019).

$\kappa = 0.15\,\mathrm{W/m\ K}$	$\rho_0 = 980\,\mathrm{kg/m^3}$	$C_p = 1600\,\mathrm{J/kg\ K}$			
$A_a = 8.55 \times 10^{15}\,1/\mathrm{s}$	$E_a = 110,750\,\mathrm{J/mol}$	$n = 1.77$	$m = 0.81$	$c_d = 14.41$	$\alpha_d = 0.41$

2.4. Boundary conditions and source terms

We now specify the external mechanical and thermal stimuli applied to the solid, which comprise of both prescribed boundary conditions and sources terms in the bulk. On a portion $\partial\Omega_0^{\mathcal{X}}$ of the boundary $\partial\Omega_0$, the deformation field χ is taken to be specified by a known function $\boldsymbol{\xi}$, while the complementary part of the boundary $\partial\Omega_0^S = \partial\Omega_0 \backslash \partial\Omega_0^{\mathcal{X}}$ is subjected to a prescribed nominal traction $\mathbf{SN} = \bar{\mathbf{t}}$. Moreover, the value of the temperature T is taken to be given by a known function $\overline{T}$ on a portion $\partial\Omega_0^{\mathcal{T}}$ of the boundary $\partial\Omega_0$, while the complementary portion $\partial\Omega_0^{\mathcal{C}} = \partial\Omega_0 \backslash \partial\Omega_0^{\mathcal{T}}$ is subjected to a prescribed normal heat flux $\mathbf{Q}\cdot\mathbf{N} = \bar{q}$. More specifically, we consider the boundary conditions

$$\begin{cases} \chi(\mathbf{X},t) = \boldsymbol{\xi}(\mathbf{X},t), \quad (\mathbf{X},t) \in \partial\Omega_0^{\mathcal{X}} \times [0,t_1] \\ \left[\dfrac{\partial\psi}{\partial\mathbf{F}}(\tilde{\mathbf{F}},\alpha)\right]\mathbf{N} = \bar{\mathbf{t}}(\mathbf{X},t), \quad (\mathbf{X},t) \in \partial\Omega_0^S \times [0,t_1] \end{cases} \tag{21}$$

and

$$\begin{cases} T(\mathbf{X},t) = \overline{T}(\mathbf{X},t), \quad (\mathbf{X},t) \in \partial\Omega_0^{\mathcal{T}} \times [0,t_1] \\ \mathbf{Q}\cdot\mathbf{N} = \bar{q}(\mathbf{X},t), \quad (\mathbf{X},t) \in \partial\Omega_0^{\mathcal{C}} \times [0,t_1] \end{cases} \tag{22}$$

Throughout Ω_0, we consider that the solid is subjected to a body force and heat source term

$$\mathbf{B}(\mathbf{X},t) \quad \text{and} \quad S(\mathbf{X},t), \quad (\mathbf{X},t) \in \Omega_0 \times [0,T]. \tag{23}$$

The heat source relevant to our problem of interest is the heat released from the exothermic chemical reaction, defined hereafter as

$$S(\mathbf{X},t) = \rho_0 H_r \frac{\partial\alpha}{\partial t}, \tag{24}$$

where H_r (= 350.0 J/g for DCPD) is the heat of reaction.

2.5. Governing equations

We can now formulate the complete theory for the thermo-chemo-mechanical response during frontal polymerization. Combining the balance Eq. (4), (6), (7) and constitutive relations (13), (19), (20) introduced above, the following governing equations are generated for the deformation field $\chi(\mathbf{X},t)$, the temperature field $T(\mathbf{X},t)$, and the degree of cure $\alpha(\mathbf{X},t)$:

$$\begin{cases} \mathrm{Div}\left[\dfrac{\partial\psi}{\partial\tilde{\mathbf{F}}}(\tilde{\mathbf{F}})\,\mathbf{F}^{\theta-1}\,\mathbf{F}^{r-1}\right] + \mathbf{B}(\mathbf{X},t) = \mathbf{0}, \quad (\mathbf{X},t) \in \Omega_0 \times [0,t_1] \\ \det\tilde{\mathbf{F}}(\mathbf{X},t) > 0, \quad (\mathbf{X},t) \in \Omega_0 \times [0,t_1], \\ \chi(\mathbf{X},t) = \boldsymbol{\xi}(\mathbf{X},t), \quad (\mathbf{X},t) \in \partial\Omega_0^{\mathcal{X}} \times [0,t_1] \\ \left[\dfrac{\partial\psi}{\partial\mathbf{F}}(\tilde{\mathbf{F}},\alpha)\right]\mathbf{N} = \bar{\mathbf{t}}(\mathbf{X},t) \quad (\mathbf{X},t) \in \partial\Omega_0^S \times [0,t_1] \end{cases} \tag{25}$$

and

$$\begin{cases} \mathrm{Div}\left[\kappa J\mathbf{F}^{-1}\mathbf{F}^{-T}\nabla T\right] + \rho_0 H_r \dfrac{\partial\alpha}{\partial t} = \rho_0 C_p \dfrac{\partial T}{\partial t}, \quad (\mathbf{X},t) \in \Omega_0 \times [0,t_1] \\ T(\mathbf{X},0) = T_0, \quad \mathbf{X} \in \Omega_0 \\ T(\mathbf{X},t) = \overline{T}(\mathbf{X},t), \quad (\mathbf{X},t) \in \partial\Omega_0^{\mathcal{T}} \times [0,t_1] \\ \mathbf{Q}\cdot\mathbf{N} = \bar{q}(\mathbf{X},t), \quad (\mathbf{X},t) \in \partial\Omega_0^{\mathcal{C}} \times [0,t_1] \end{cases} \tag{26}$$

and

$$\begin{cases} \dfrac{\partial\alpha}{\partial t} = A_a \exp\left(\dfrac{-E_a}{RT}\right)(1-\alpha)^n\alpha^m \dfrac{1}{1+\exp(c_d(\alpha-\alpha_d))}, \quad (\mathbf{X},t) \in \Omega_0 \times [0,t_1] \\ \alpha(\mathbf{X},0) = \alpha_0, \quad \mathbf{X} \in \Omega_0 \end{cases} \tag{27}$$

3. Numerical implementation and verification

In this section, we first present a finite-element formulation to solve the coupled system of Eqs. (25)–(27). The major challenge here is the selection of an appropriate finite-element discretization capable of dealing with the large deformations and near incompressibility of the gel. We begin by recasting the strong form of the governing equations into a weak form. The cure kinetic Eq. (27) will be solved at the quadrature points after space discretization and is hence not recasted into weak form.

Upon definition of admissible sets

$$\mathcal{U} = \left\{\mathbf{y} \in W^{1,2}(\Omega_0;\mathbb{R}^N) : \mathbf{y} = \boldsymbol{\xi} \text{ on } \partial\Omega_0^{\mathcal{X}}\right\}, \quad \mathcal{U}_0 = \left\{\mathbf{y} \in W^{1,2}(\Omega_0;\mathbb{R}^N) : \mathbf{y} = \mathbf{0} \text{ on } \partial\Omega_0^{\mathcal{X}}\right\},$$
$$\mathcal{V} = \left\{z \in W^{1,2}(\Omega_0;\mathbb{R}^N) : z = \overline{T} \text{ on } \partial\Omega_0^{\mathcal{T}}\right\}, \quad \mathcal{V}_0 = \left\{z \in W^{1,2}(\Omega_0;\mathbb{R}^N) : z = 0 \text{ on } \partial\Omega_0^{\mathcal{T}}\right\},$$

the boundary value problems (25)–(26) can be reformulated as the problem of finding the deformation field $\chi \in \mathcal{U}$, temperature field $T \in \mathcal{V}$ and degree of cure field $\alpha \in L^2(\Omega_0)$ such that

$$\int_{\Omega_0} \left[\frac{\partial \psi}{\partial \mathbf{F}}(\tilde{\mathbf{F}})\right] \cdot \nabla \mathbf{v}\, d\mathbf{X} - \int_{\Omega_0} \mathbf{b} \cdot \mathbf{v}\, d\mathbf{X} - \int_{\partial\Omega_0^S} \bar{\mathbf{t}} \cdot \mathbf{v}\, d\mathbf{X} = 0 \quad \forall \mathbf{v} \in \mathcal{U}_0,\ t \in [0, t_1], \tag{28}$$

and

$$\int_{\Omega_0} \left[\kappa J \mathbf{F}^{-1}\mathbf{F}^{-T}\nabla T\right] \cdot \nabla P\, d\mathbf{X} + \int_{\Omega_0} \left(\rho_0 C_p \frac{\partial T}{\partial t} - \rho_0 H_r \frac{\partial \alpha}{\partial t}\right) P\, d\mathbf{X} - \int_{\partial\Omega_0^C} \overline{Q}\, P\, d\mathbf{X} = 0 \quad \forall P \in \mathcal{V}_0,\ t \in [0, t_1]. \tag{29}$$

3.1. Time and space discretizations

We first partition the time interval under consideration $[0, t_1]$ in the Eqs. (28)–(29) into discrete times $0 = t^0, t^1, \ldots t^m, t^{m+1}, \ldots, t^M = t_1$ together with the notation $\chi^m(\mathbf{X}) = \chi(\mathbf{X}, t^m)$, $T^m(\mathbf{X}) = T(\mathbf{X}, t^m)$, and $\alpha^m(\mathbf{X}) = \alpha(\mathbf{X}, t^m)$ for $m = 0, 1, 2, \ldots, M$. We then adopt the implicit Euler scheme to cast the weak form of the governing equations into their time-discretized form.

For the spatial discretization, we consider partitions ${}^h\Omega_0 = \bigcup_{e=1}^{\mathtt{N}_e} \mathcal{E}^{(e)}$ with $\mathcal{E}^{(i)} \cap \mathcal{E}^{(j)} = \varnothing\ \forall i \neq j$ of the domain Ω_0 that comprise $\mathtt{N}_e$ non-overlapping simplicial elements $\mathcal{E}^{(e)}$, with h denoting the diameter of the largest element. We discretize the deformation field over each simplicial elements $\mathcal{E}^{(e)}$ with Crouzeix–Raviart (C-R) linear shape functions, as these non-conforming finite-element discretizations have been shown to be stable and convergent under near incompressibility and large deformations with fewer degrees of freedom than competing conforming dicretizations (Kumar et al., 2018). The C-R shape functions are $N^{(1)}_{CR}(\rho_1, \rho_2) = 1 - 2\rho_2$, $N^{(2)}_{CR}(\rho_1, \rho_2) = 2(\rho_1 + \rho_2) - 1$, $N^{(3)}_{CR}(\rho_1, \rho_2) = 1 - 2\rho_1$ for the case of $N = 2$ space dimensions, and $N^{(1)}_{CR}(\rho_1, \rho_2, \rho_3) = 1 - 3\rho_3$, $N^{(2)}_{CR}(\rho_1, \rho_2, \rho_3) = 3(\rho_1 + \rho_2 + \rho_3) - 1$, $N^{(3)}_{CR}(\rho_1, \rho_2, \rho_3) = 1 - 3\rho_1$, $N^{(4)}_{CR}(\rho_1, \rho_2, \rho_3) = 1 - 3\rho_2$ for the case of $N = 3$ space dimensions, where ρ_i are the coordinates of a reference simplicial element. For the temperature field, we adopt the standard linear Lagrange shape functions.

3.2. The solver: staggered scheme

After the discretization of the governing PDEs (25)–(27), the next step is to select an appropriate solver for the resulting system of three coupled nonlinear algebraic equations respectively denoted as $\mathcal{G}_1$, $\mathcal{G}_2$, $\mathcal{G}_3$. A monolithic solution scheme for our choice of cure kinetics relation (20) requires a very small mesh size and time step, so we instead adopt a staggered approach. Specifically, the algorithm to solve for the approximate solution fields ${}^h\chi^{m+1}$, ${}^hT_i^{m+1}$, and ${}^h\alpha^{m+1}$ at t^{m+1} is as follows:

- *Step 0.* Set the staggered iteration counter $r = 1$ and define appropriate tolerances $TOL_1 > 0$ and maximum number of iterations $\mathtt{I}_1$. For a given solution ${}^h\chi^m$, ${}^hT^m$, and ${}^h\alpha^m$ at time t^m, define also ${}^h\chi^{m+1,0} = {}^h\chi^m$, ${}^hT^{m+1,0} = {}^hT^m$, and ${}^h\alpha^{m+1,0} = {}^h\alpha^m$.
- *Step 1.* At the Gauss quadrature points in each of the simplicial elements, find ${}^h\alpha^{m+1,r}$ such that

$$\mathcal{G}_3({}^hT^{m,r}, {}^h\alpha^{m+1,r}) = 0. \tag{30}$$

- *Step 2.* Having solved the sub-problem (30) for ${}^h\alpha^{m+1,r}$, which provides the heat source term, and given the increments $\overline{T}^{m+1}(\mathbf{X})$ and $\overline{Q}^{m+1}(\mathbf{X})$ in boundary data, find ${}^hT^{m+1,r}$ such that

$$\mathcal{G}_2({}^h\chi^{m,r}, {}^hT^{m+1,r}, {}^h\alpha^{m+1,r}) = 0. \tag{31}$$

- *Step 3.* Having solved the sub-problems (30) and (31) for ${}^h\alpha^{m+1,r}$ and ${}^hT^{m+1,r}$, update the eigenstrains $\mathbf{F}^{\theta^{m+1,r}}$ and $\mathbf{F}^{r^{m+1,r}}$, and the elastic properties E and ν at the quadrature points. Then, given the increments $\boldsymbol{\xi}^{m+1}(\mathbf{X})$, $\bar{\mathbf{t}}^{m+1}(\mathbf{X})$, and $\mathbf{b}^{m+1}(\mathbf{X})$ in boundary data and body force, find ${}^h\chi^{m+1,r}$ such that

$$\mathcal{G}_1({}^h\chi^{m+1,r}, {}^hT^{m+1,r}, {}^h\alpha^{m+1,r}) = 0. \tag{32}$$

- *Step 4.* If $\| \mathcal{G}_1({}^h\chi_j^{m+1,r}, {}^hT^{m+1,r}, {}^h\alpha^{m+1,r}) \| / \| \mathcal{G}_1({}^h\chi_j^{m+1,0}, {}^hT^{m+1,0}, {}^h\alpha^{m+1,r}) \| \leq TOL_1$ or $r > \mathtt{I}_1$, then set ${}^h\chi^{m+1} = {}^h\chi^{m+1,r}$, ${}^hT^{m+1} = {}^hT^{m+1,r}$, ${}^h\alpha^{m+1} = {}^h\alpha^{m+1,r}$ and move to the next time step t^{m+2}; otherwise set $r \leftarrow r + 1$ and go back to Step 1.

Sub-problems (30) and (32) are nonlinear and thus solved with Newton's method, while sub-problem (31) is linear.

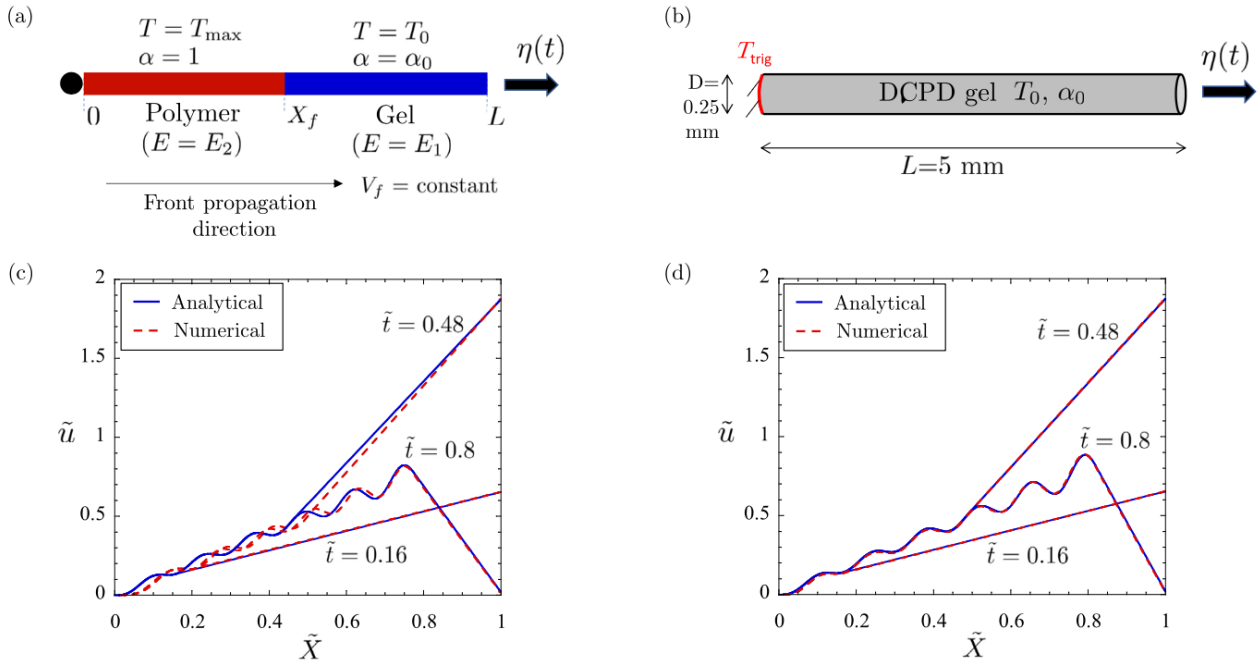

Fig. 4. Verification study for the numerical implementation of the theory outlined in Sections 3.1 and 3.2. (a) Schematic of the idealized 1-D specimen geometry fixed at $X = 0$ and subjected to time-dependent loading $\eta(t)$ at $X = L$. The reaction front located at $X_f(t)$ is assumed to be of zero width and to propagate at a constant speed V_f. The reaction front separates the polymerized region (in red) and the gel region (in blue). For both regions, the temperature and degree of cure are known exactly. (b) Schematic of the 3-D bar problem solved with the proposed numerical scheme. The applied boundary and initial conditions are also shown. (c) Comparison between numerical results obtained using material properties described in Section 2.3 and analytical results for the idealized problem at three different times for applied loading $\eta(t) = A(1 - \cos(10t))$ with $A = 0.01$ mm. The normalized displacement $\tilde{u}$ is defined as $\tilde{u} = u/(A)$ and the normalized coordinate as $\tilde{X} = X/L$. (d) Comparison between numerical results obtained using a simplified cure kinetic model (39) and analytical results.

3.3. Verification problem

Next, we verify the proposed numerical formulation by solving an idealized 1-D problem for which an analytical solution can be derived. The verification problem is shown schematically in Fig. 4(a) and is based on the following assumptions:

- Deformations in the structure at all times are small, i.e., $\mathbf{F}(\mathbf{X}, t) \to \mathbf{I}$.
- The thermal and reaction fronts coincide with each other at location $X_f(t)$ and are mathematically sharp. For $X > X_f$, $T = T_0$ and $\alpha = \alpha_0$. For $X \leq X_f$, $T = T_{\max}$ and $\alpha = 1$.
- The front propagates at a steady speed V_f for $t \geq 0$, which corresponds to the chosen value of T_0 and α_0.
- There is no heat loss from the domain.

Under the above assumptions, the governing equations reduce to

$$\begin{cases} \dfrac{\partial}{\partial X}(E(X)\,\tilde{\varepsilon}) = 0, \quad (X,t) \in [0,L] \times [0,t_1] \\ \chi(0,t) = 0, \quad \chi(L,t) = \eta(t), \quad t \in [0,t_1], \\ T = T_{\max}, \quad (X,t) \in [0,X_f] \times [0,t_1], \quad T = T_0, \quad (X,t) \in [X_f,L] \times [0,t_1], \\ \alpha = 1, \quad (X,t) \in [0,X_f] \times [0,t_1], \quad \alpha = \alpha_0 \quad (X,t) \in [X_f,L] \times [0,t_1] \end{cases} \tag{33}$$

where $\tilde{\varepsilon} = \partial u/\partial X - \varepsilon^\theta - \varepsilon^r$ and $T_{\max} = T_0 + (1 - \alpha_0)H_r/C_p$. The elastic modulus $E(X) = E_2$ in the polymerized region ($X \leq X_f$) and $E(X) = E_1$ in the gel region ($X > X_f$) as shown in Fig. 4(a). The eigenstrain due to thermal expansion ε^θ is equal to $\varepsilon^\theta = \zeta(T - T_0)$, whereas the eigenstrain associate with curing ε^r in the small-deformation limit reduces to

$$\boldsymbol{\varepsilon}^r(X,t) = \begin{cases} \partial u/\partial X(X^+, t^*) - \zeta(T_{\max} - T_0), & \text{if } t \geq t^* \\ 0, & \text{otherwise} \end{cases}$$

where $t^* = X/V_f$ denotes the time at which the front arrives at location X. From $(33)_1$, it follows that, in the region $X \in (X_f, L]$,

$$\frac{\partial}{\partial X}(E_1(\varepsilon^e(X,t))) = 0 \quad \Rightarrow \quad \varepsilon^e(X,t) = {\varepsilon_1}^e(t), \tag{34}$$

whereas, in the region $X \in [0, X_f)$,

$$\frac{\partial}{\partial X}(E_2(\varepsilon^e(X,t) - \zeta\Delta T - {\varepsilon_1}^e(X/V_f))) = 0, \tag{35}$$

with $\Delta T = T_{\max} - T_0$. At the gel-polymer interface at $X = X_f$, we have traction continuity:

$$E_2(\varepsilon^e(X,t) - \zeta\Delta T - {\varepsilon_1}^e(X/V_f)) = E_1{\varepsilon_1}^e(t) \tag{36}$$

Solving (35)–(36) along with the boundary conditions $(33)_2$, we obtain an integral equation for ${\varepsilon_1}^e(t)$

$$\eta(t)L_0 - {\varepsilon_1}^e(t)\,(L_0 - X_f) = \frac{E_1}{E_2}\,{\varepsilon_1}^e(X_f/V_f)\,X_f + \zeta\Delta T\,X_f + \int_0^{X_f} {\varepsilon_1}^e(y/V_f)\,dy. \tag{37}$$

Eq. (37) can be equivalently written in a non-dimensional differential form

$$\left(\left(\frac{E_1}{E_2} - 1\right)\tilde{t} + 1\right)\frac{d{\varepsilon_1}^e}{d\tilde{t}} + \frac{E_1}{E_2}\,{\varepsilon_1}^e = -\zeta\Delta T + \frac{d\eta}{d\tilde{t}}, \tag{38}$$

where $\tilde{t} = \dfrac{t}{t_{\max}}$ with $t_{\max} = L/V_f$. Eq. (38) is a linear first-order ordinary differential equation that can be solved analytically or semi-analytically for arbitrary expressions of the loading function $\eta(\tilde{t})$. For example, for $\eta(\tilde{t}) = A\,(1 - \cos(\omega\tilde{t}))$, the solution is

$$\begin{aligned}
{\varepsilon_1}^e(\tilde{t}) = \frac{e^{-\frac{i\omega}{E_r-1}}\left(\left(E_r-1\right)\tilde{t}+1\right)^{-\frac{E_r}{E_r-1}}}{2E_r}\Bigg[&-2\alpha\Delta T e^{\frac{i\omega}{E_r-1}}\left(\left(\left(E_r-1\right)\tilde{t}+1\right)^{\frac{E_r}{E_r-1}} - 1\right) - \\
&\frac{iA\omega E_r}{E_r-1}\left(\mathrm{Ei}\left[\frac{1}{1-E_r}, -\frac{i\omega}{E_r-1}\right] - e^{\frac{2i\omega}{E_r-1}}\mathrm{Ei}\left[\frac{1}{1-E_r}, \frac{i\omega}{E_r-1}\right] + \right. \\
&\left(\left(E_r-1\right)\tilde{t}+1\right)^{\frac{E_r}{E_r-1}}\left(e^{\frac{2i\omega}{E_r-1}}\mathrm{Ei}\left[\frac{1}{1-E_r}, (i\omega)\left(\tilde{t} + \frac{1}{E_r-1}\right)\right] - \right. \\
&\left.\left.\left.\mathrm{Ei}\left[\frac{1}{1-E_r}, -\frac{i\omega\left(\left(E_r-1\right)\tilde{t}+1\right)}{E_r-1}\right]\right)\right)\Bigg],
\end{aligned}$$

where $E_r = E_1/E_2$ and the function $\mathrm{Ei}\,[a,b]$ is given by $\mathrm{Ei}\,[a,b] = \int_1^\infty e^{-bt}/t^a\,dt$. Once ${\varepsilon_1}^e$ is known, the normalized displacement field $\tilde{u}(\tilde{X},\tilde{t})$, where $\tilde{X} = X/L$, can be obtained as

$$\tilde{u}(\tilde{X},\tilde{t}) = \frac{u(\tilde{X},\tilde{t})}{A} = \begin{cases} \dfrac{1}{A}\left(\dfrac{E_1}{E_2}\,{\varepsilon_1}^e\left(\dfrac{X_f(\tilde{t})}{V_f}\right)\tilde{X} + \zeta\Delta T\tilde{X} + \int_0^{\tilde{X}} {\varepsilon_1}^e\left(\dfrac{y}{V_f}\right)dy\right), & \text{if } \tilde{X} \in [0, X_f/L] \\ 1 - \cos(\omega\tilde{t}) - \dfrac{1}{A}{\varepsilon_1}^e\left(\dfrac{X_f(\tilde{t})}{V_f}\right)(1-\tilde{X}), & \text{if } \tilde{X} \in [X_f/L, 1] \end{cases}$$

We present the analytical results for the normalized displacement field for three different times $\tilde{t} = 0.16, 0.48$, and 0.8 in Fig. 4(c). At $\tilde{t} > c$, the front is located in the normalized coordinates $\tilde{X}_f = X_f/L$ at $\tilde{X}_f = c$. The analytical results show that $\tilde{u}(\tilde{X},\tilde{t})$ for $\tilde{t} > c$ remain unchanged for the domain $\tilde{X} \le c$, illustrating the freezing of deformations brought upon by curing.

To verify our proposed finite-element discretization and the staggered solver outlined in the previous two subsections, we also solve the problem of a three-dimensional bar subjected to cyclic loading using 2-D axisymmetric finite elements (Fig. 4(b)). The bar is taken to be of length $L = 5$ mm and diameter $D = 0.25$ mm. At $X = L$, we apply the cyclic loading $\eta(t) = A\,(1 - \cos(\hat{\omega}t))$ with $A = 0.01$ mm and $\hat{\omega} = \omega/t_{\max} = 10\ \mathrm{s}^{-1}$. At $X = 0$, the bar is held fixed and a temperature trigger $T_{\mathrm{trig}} = 230°\mathrm{C}$ is applied for 1 s. The initial temperature T_0 and initial degree of cure α_0 are chosen to be 30°C and 0.1 respectively. The analytical results show that $\tilde{u}(\tilde{X},\tilde{t})$ for $\tilde{t} > c$ remain unchanged for $\tilde{X} \le c$, illustrating the freezing of deformations brought upon by curing.

The numerical results for the axial displacement field from solving Eqs. (25)–(27) for the material properties outlined in Section 2.3 are also presented in Fig. 4(c). The numerical problem does not adhere perfectly to the idealizations of the 1-D theoretical solution, i.e., the front is mathematically sharp and propagates at a steady speed. Yet, the results show a reasonable agreement with the analytical results obtained for the idealized problem. To further confirm the accuracy of the proposed numerical scheme and also the regularization adopted for the eigenstrain $\mathbf{F}^r$ (10)–(12), we also solved the numerical problem with a different cure kinetics model for which the front width is much smaller. In this model, the function $h(T,\alpha)$ in the cure kinetic relation (7) is given by

$$h(T,\alpha) = A_a\,\exp\left(\frac{-E_a}{RT}\right)(1-\alpha)^n, \tag{39}$$

with the values $A_a = 1.54 \times 10^{12}\ 1/\mathrm{s}$, $E_a = 92,800\,\mathrm{J/mol}$, and $n = 2.3$ obtained by fitting differential scanning calorimetry (DSC) data for DCPD. The numerical results for the axial displacement field using the simplified model (39) are presented in Fig. 4(d), and show excellent agreement with the analytical results.

4. Numerical results

In this section, we explore the capabilities of this theory to describe the coupled thermo-chemo-mechanical response of a frontally polymerizing gel specimen under constant and oscillatory loads. For computational frugality, the simulations in this section are conducted in 2-D under the assumption of plane strain. First, we discuss the effect of mechanical loading on the speed and stability of the polymerization front. Then, we investigate how changing the oscillatory loading affects the induced surface pattern. Finally, we show how non-steady mechanical loading can accentuate the thermo-chemical instabilities inherent in the FP process and lead

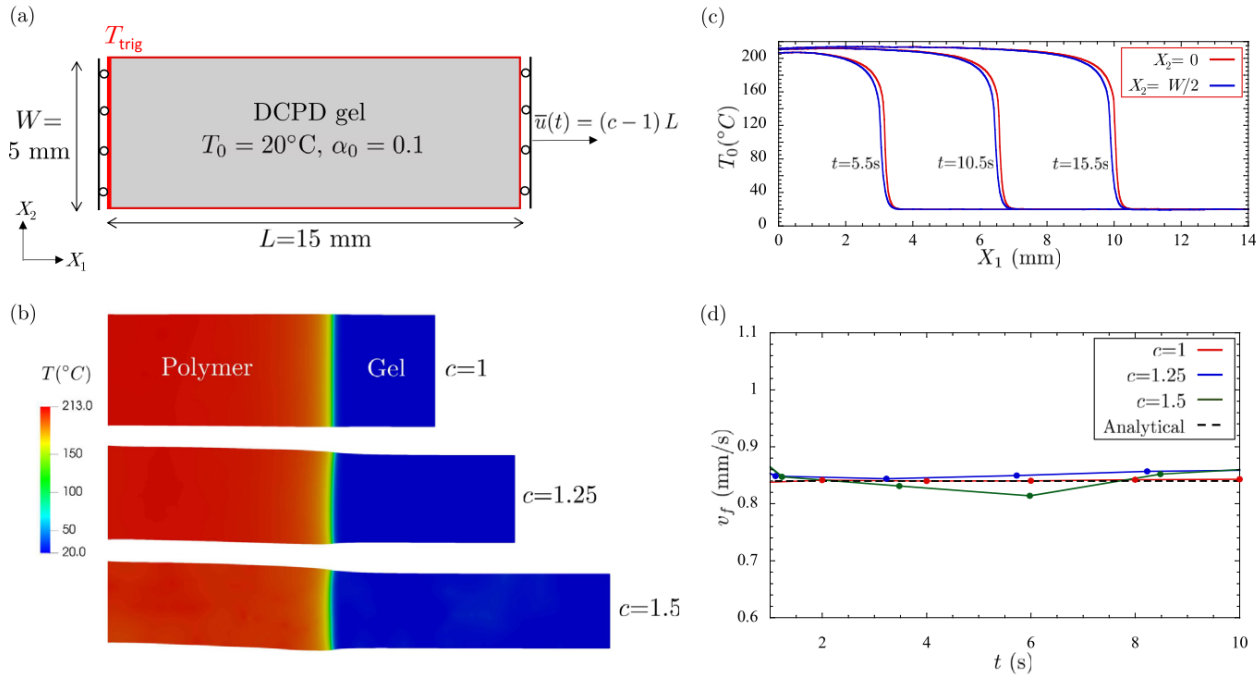

Fig. 5. Simulation of frontal polymerization conducted under a constant pre-applied stretch of $c = 1, 1.25$ and 1.5. (a) Schematic of the specimen geometry in its initial configuration at $t = 0$, and applied boundary and initial conditions. (b) Contour plots of the temperature field $T(\mathbf{x}, t)$ at $t = 12$ s for the three cases. (c) Temperature profiles along the direction of front propagation shown for the case of applied stretch 1.25 and along two parallel planes: bottom plane ($X_2 = 0$) and middle plane ($X_2 = W/2$). (d) True velocity as a function of time for the three cases: comparison between numerical (solid curves) and analytically expected value.

to a more complex surface pattern. All of the simulations are carried out over a fixed rectangular domain of dimensions $L \times W =$ 15 mm × 5 mm under adiabatic conditions. The reaction front is triggered by applying temperature $T_{\text{trig}} = 210°\text{C}$ for 1 s along the left boundary of the domain $X = 0$ while the mechanical loading is applied at the right boundary $X = L$. The elastic, thermal, and cure kinetic properties for DCPD are as listed in Section 2.3.

4.1. FP in DCPD gel specimen under constant pre-applied stretch

We begin with the simulation for the case in which frontal polymerization is conducted under a constant pre-applied displacement $\bar{u} = (c-1)\,L$. A schematic of the geometry is shown in Fig. 5(a). Three values of applied stretch are studied: $c = 1, 1.25$, and 1.5. Fig. 5(b) shows the contour plots for the temperature field in the *deformed* configuration, i.e., $T(\mathbf{x}, t)$, at $t = 12$ s for each of the three cases. The location of the front plane is nearly identical for the three cases, which shows that the true or spatial front velocity is unaffected by mechanical loading as expected from Eq. (5). Experiments have also confirmed the previous observation as discussed in Section 5.5.

Fig. 5(c) shows the temperature profiles at three different times $t = 5.5, 10.5$, and 15.5 s for $c = 1.25$ in the direction of front propagation along two planes: bottom plane ($X_2 = 0$) and middle plane ($X_2 = W/2$). As apparent there, the front propagates in a stable manner. Since the deformation is not exactly homogeneous in the domain because of thermal expansion, the front is slightly ahead in the bottom plane compared to the middle plane. We further explore the speed of the reaction front quantitatively in Fig. 5(d), which presents the true velocity v_f as a function of time for each of the three loading cases, with v_f defined as

$$v_f = \frac{dx_f(t)}{dt} \quad \text{where} \quad x_f(t) = \mathbf{x}(t)|_{(X_2 = W/2, \alpha = 0.5)} \cdot \mathbf{e}_1. \tag{40}$$

The results show that the true velocity is nearly independent of the amount of pre-stretching even under fairly large deformations and is equal to 0.84 mm/s on an average, which matches the front velocity v obtained from the solution of the thermo-chemical equations in the absence of structural deformations obtained either numerically or from the analytical solution for front velocity presented in Kumar et al. (2021).

Note, however, that the material frame velocity defined as:

$$V_f = \frac{dX_f(t)}{dt} \quad \text{where} \quad X_f(t) = \mathbf{X}(t)|_{(X_2 = W/2, \alpha = 0.5)} \cdot \mathbf{e}_1 \tag{41}$$

depends on the amount of pre-stretching. This effect can be observed from the governing Eq. (26) written in the material frame, which shows a dependence of the thermal-chemical solution on the deformation gradient tensor $\mathbf{F}$. Based on the governing Eq. (26),

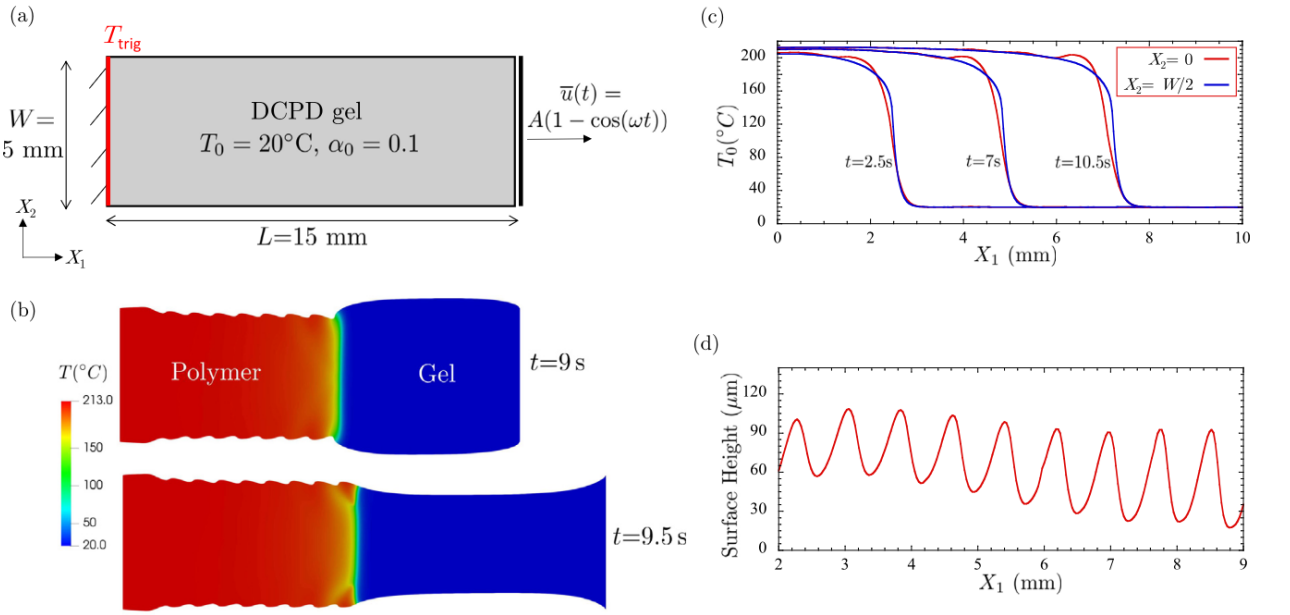

Fig. 6. Simulation of FP under simultaneous cyclic loading and at room temperature. (a) Schematic of the specimen geometry in its initial configuration and applied boundary and initial conditions. (b) Contour plots of the temperature field in the deformed configuration for $A = 0.05\,L$ at $t = 9$ s and $t = 9.5$ s illustrating the formation of a surface pattern. (c) Temperature profiles along the direction of front propagation along two planes: bottom plane ($X_2 = 0$) and middle plane ($X_2 = W/2$) showing the oscillatory loading-induced instabilities. (d) Height of the surface pattern, i.e., spatial variation of the post-FP displacement of the top edge of the specimen.

we can define an effective thermal conductivity tensor $\mathbf{K}$ as

$$\mathbf{K} = \kappa J \mathbf{F}^{-1}\mathbf{F}^{-T}. \tag{42}$$

From the analytical solution for the thermo-chemical equations, we know that the front velocity of a unidirectional front is proportional to the square root of the thermal conductivity in the direction of the front, i.e., $V_f \propto \sqrt{K_{11}}$. Hence, for known values of tensor $\mathbf{F}$, we can readily estimate the material frame front velocity for different values of pre-stretching. For $c = 1$, $V_f = v_f$. For the cases $c = 1.25$ and $c = 1.5$, as $F_{11} = c$, the material frame front velocity is predicted to be approximately $v_f/1.25$ and $v_f/1.5$, respectively.

4.2. FP in DCPD gel specimen subjected to simultaneous oscillatory loading

Next, we focus our attention on the case in which FP is conducted in the specimen under simultaneous uniaxial oscillatory loading. A schematic of the geometry along with the boundary and initial conditions is shown in Fig. 6(a). The initial temperature of the gel is assumed to be $T_0 = 20°C$. The applied displacement at the right boundary is taken to be $\bar{u} = A(1 - \cos(\omega t))$ with $A = 0.05\,L = 0.75$ mm and $\omega = 1$ Hz.

Fig. 6(b) shows the contour plots for the temperature field in the deformed configuration, $T(\mathbf{x}, t)$, at $t = 9$ s and $t = 9.5$ s. We observe that, while the polymerization front propagates in a steady, stable fashion at that initial temperature in the absence of the cyclic loading (see Fig. 5(c)), the coupling between the deformation field and the thermo-chemical fields leads to a two-head front instability originating from the top and bottom edges of the domain. This instability can be better visualized in Fig. 6(c), which presents the temperature profiles along the direction of front propagation along the bottom edge ($X_2 = 0$) and the middle plane ($X_2 = W/2$).

Fig. 6(d) shows the height of the surface pattern after the completion of the FP process. We note that the amplitude of the pattern increases with X_1 and that the surface pattern is asymmetric in its peaks and valleys despite a sinusoidal applied input.

To visualize the residual deformations inside the domain, we show in Fig. 7 contour plots of the maximum eigenvalue $\lambda^{\max}$ of the deformation gradient tensor $\mathbf{F}$ and of the two eigenstrain tensors $\mathbf{F}^{\theta}$ and $\mathbf{F}^{r}$. The regions of tension and compression induced by the sinusoidal loading can be seen in Fig. 7(a) and Fig. 7(c) for $\lambda^{\max}_{\mathbf{F}}$ and $\lambda^{\max}_{\mathbf{F}^r}$, respectively. These regions are vertically nearly-uniform except near the top and bottom edges. The plot for $\lambda^{\max}_{\mathbf{F}^\theta}$ in Fig. 7(b) shows a higher value near the top and bottom edges, which is a consequence of the front instability discussed above in the context of Fig. 6(c).

The nature of the surface pattern is directly related to the amplitude and the frequency of the applied loading. Fig. 8(a) shows the height of the surface pattern along the direction of front propagation X_1 for three values of imposed amplitude $A_i = L/40, L/20, L/10$, whereas Fig. 8(b) presents the height of the surface pattern for three values of imposed frequency $\omega_i = 0.5, 1, 2$ Hz showing a strong dependence of the amplitude and wavelength of the surface pattern on the imposed frequency. A direct comparison with the experimental results regarding the dependence of surface pattern on the imposed frequency will be presented in the next section.

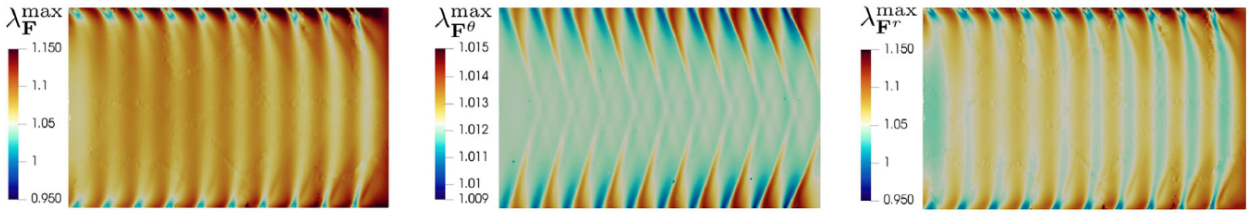

Fig. 7. Contour plots of the maximum eigenvalues $\lambda^{\max}$ of the deformation gradient tensor $\mathbf{F}$ and the two eigenstrains $\mathbf{F}^\theta$ and $\mathbf{F}^r$ shown in the reference configuration for $X_1 \in [1.5, 9.5]$ mm for the simulation of FP in a DCPD gel specimen under simultaneous cyclic loading at room temperature. (a) $\lambda^{\max}_{\mathbf{F}}$ of tensor $\mathbf{F}$, (b) $\lambda^{\max}_{\mathbf{F}^\theta}$ of tensor $\mathbf{F}^\theta$, and (c) $\lambda^{\max}_{\mathbf{F}^r}$ of tensor $\mathbf{F}^r$.

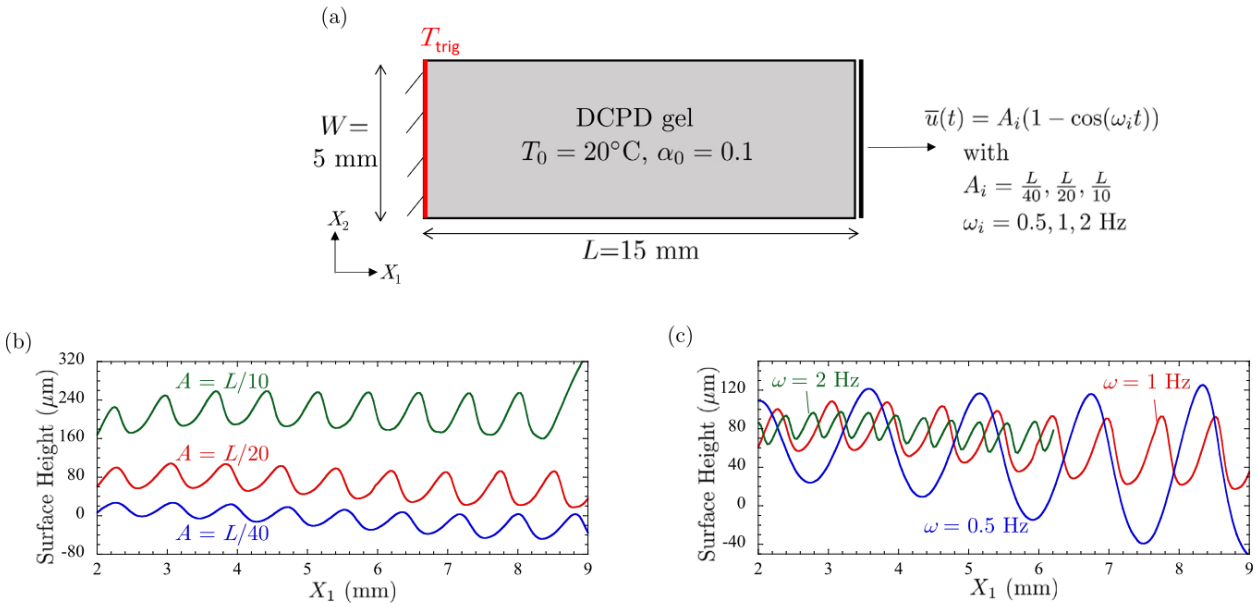

Fig. 8. FP at room temperature conducted under simultaneous oscillatory loading with three different values of the loading amplitude and frequency. (a) Schematic of the specimen geometry in its initial configuration and of the applied boundary and initial conditions. Spatial variation of the height of the surface pattern for three values of the imposed amplitude $A_i = L/40, L/20, L/10$ (b) and of the imposed frequency $\omega_i = 0.5, 1, 2$ Hz (c).

4.3. FP in DCPD gel specimen under cyclic loading at lower initial temperature

We finally turn to the case where the frontal polymerization is conducted in the gel specimen at a lower ambient temperature of $T_0 = 0°\text{C}$ while subjected to simultaneous oscillatory loading (Fig. 9(a)). For this lower initial temperature, the DCPD reaction front is known to experience a thermo-chemical instability as discussed in Goli et al. (2020). They showed that for initial temperature $T_0 < 14°\text{C}$, the front experiences a repeatable sharp thermal spike prior to achieving its final temperature as it propagates through the reaction channel. We aim to investigate how the intrinsic thermo-chemical instability interacts with the oscillatory mechanical loading.

The applied displacement at the right boundary is again taken to be $\bar{u} = A\,(1 - \cos(\omega t))$ with $A = 0.05\,L = 0.75$ mm and $\omega = 1$ Hz. Fig. 9(b) shows the contour plots for the temperature field in the deformed configuration, i.e., $T(\mathbf{x}, t)$, at $t = 20$ s and $t = 20.5$ s. It is clear that the thermal front appears to be more complex than in the previous simulation with $T_0 = 20°\text{C}$. Fig. 9(c) shows the temperature profiles along the direction of front propagation along two planes: bottom plane ($X_2 = 0$) and middle plane ($X_2 = W/2$). In contrast to Fig. 5(c) and Fig. 6(c), the temperature profile along the middle plane also shows a front instability in this case. Moreover, for the bottom plane, the front is more unstable than in Fig. 6(c). The interaction between the intrinsic thermo-chemical instability and the mechanical fields thus seems to have accentuated the front instability.

Fig. 9(d) shows the height of the surface pattern along the top edge of the specimen. As apparent in that figure, the surface pattern is also more 'chaotic' and has a smaller amplitude than in the previous case. The increased complexity of the thermo-chemo-structural solution is apparent in Fig. 10, which shows contour plots of the maximum eigenvalues $\lambda^{\max}$ of $\mathbf{F}$, $\mathbf{F}^\theta$, and $\mathbf{F}^r$. Again, in contrast to the results for $T_0 = 20°\text{C}$ shown in Fig. 7, the pattern of residual deformation observed in Fig. 10 is more irregular and intricate.

5. Experimental methodology and comparisons between experiments and theory

The numerical experiments presented in the last section illustrated the capability of the proposed theory and its numerical implementation to capture the coupled thermo-chemo-mechanical response of gels during FP under oscillatory loading. In this

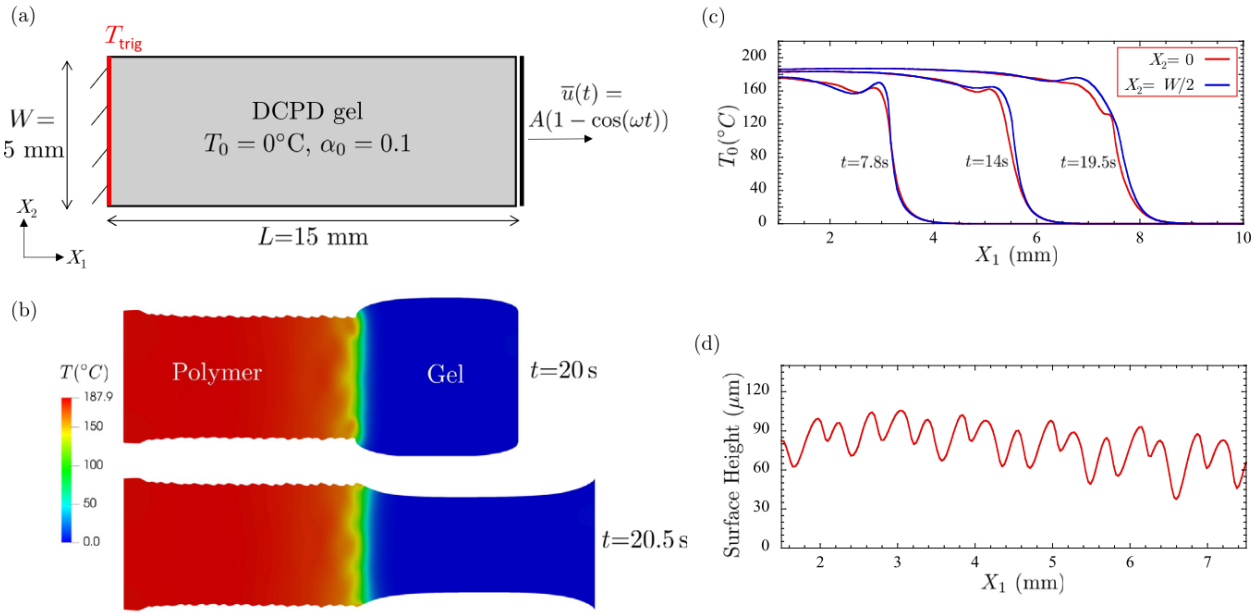

Fig. 9. FP under simultaneous cyclic loading for a lower initial temperature $T_0 = 0°C$. (a) Schematic of the specimen geometry and of the applied boundary and initial conditions. (b) Contour plots of the temperature field in the deformed configuration for $A = 0.05\,L$ at $t = 20$ s and $t = 20.5$ s demonstrating a more chaotic surface pattern. (c) Temperature profiles along two planes: bottom plane ($X_2 = 0$) and middle plane ($X_2 = W/2$), both of which show an unstable front. (d) Height of the post-FP surface pattern along the direction of front propagation.

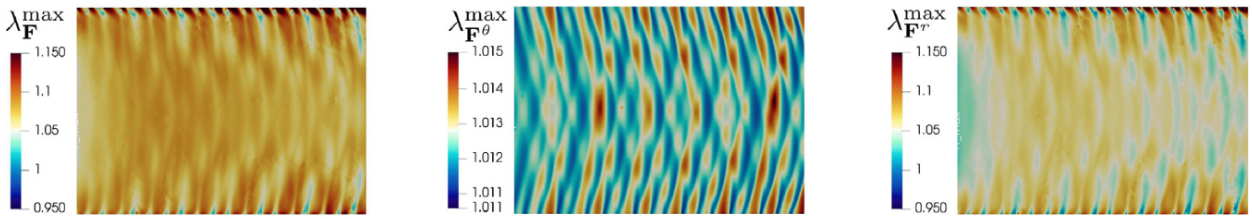

Fig. 10. Contour plots for the maximum eigenvalue (a) $\lambda_{\mathbf{F}}^{max}$ of tensor $\mathbf{F}$, (b) $\lambda_{\mathbf{F}^\theta}^{max}$ of tensor $\mathbf{F}^\theta$, and (c) $\lambda_{\mathbf{F}^r}^{max}$ of tensor $\mathbf{F}^r$, shown in the region $X_1 \in [1, 8]$ mm for the simulation of frontal polymerization conducted under simultaneous cyclic loading and low initial temperature $T_0 = 0$ °C.

section, we aim to provide more quantitative evidence for the descriptive and predictive capabilities of the theory by making direct comparisons with a new set of experiments. We focus on the investigation of surface patterns formed by applying a uniaxial oscillatory load during FP of a partially cured DCPD gel. Below, we first present our experimental methodology including the characterization techniques. The experimental results are then compared directly with results from 3-D simulations.

5.1. Materials

Dicyclopentadiene (DCPD), 5-ethylidene-2-norbornene (ENB), 2nd generation Grubbs' catalyst (GC2), and phenylcyclohexane (PCH) were purchased from SigmaAldrich. Since DCPD is solid at room temperature, 5 wt % ENB was added to depress the melting point below room temperature and facilitate handling. All references to DCPD in this work refer to this 95:5 DCPD:ENB mixture. Tributyl phosphite (TBP) inhibitor was purchased from TCI Chemicals and stored under inert gas. All other chemicals were used as received.

5.2. Preparation of DCPD gel samples

Liquid resin was prepared by mixing the appropriate amount of DCPD with GC2 and TBP, using PCH as a solvent. For a typical sample, GC2 (12.5 mg, 14.7 μmol) was dissolved in PCH (625 μL) using bath sonication (10 min). TBP (4.0 μL, 14.7 μmol, 1 equiv) was added, and the solution was then thoroughly mixed with DCPD (19.46 g, 147 mmol, 10000 equiv). The low-viscosity liquid resin was carefully poured into a rectangular cell casting mold consisting of borosilicate glass plates and a polyurethane spacer. The resin was then pre-cured, either in ambient conditions (ca. 20°C) or in an oven set to 30°C. The pre-curing time dictated the degree of pre-cure (α_0) and stiffness of the gel. The degree of pre-cure, in turn, affects the velocity of the polymerization front. Typical pre-curing times were 6–9 h at 20°C, or 2.5–3.5 h at 30°C. After pre-curing, the gel was removed from the mold and cut to size.

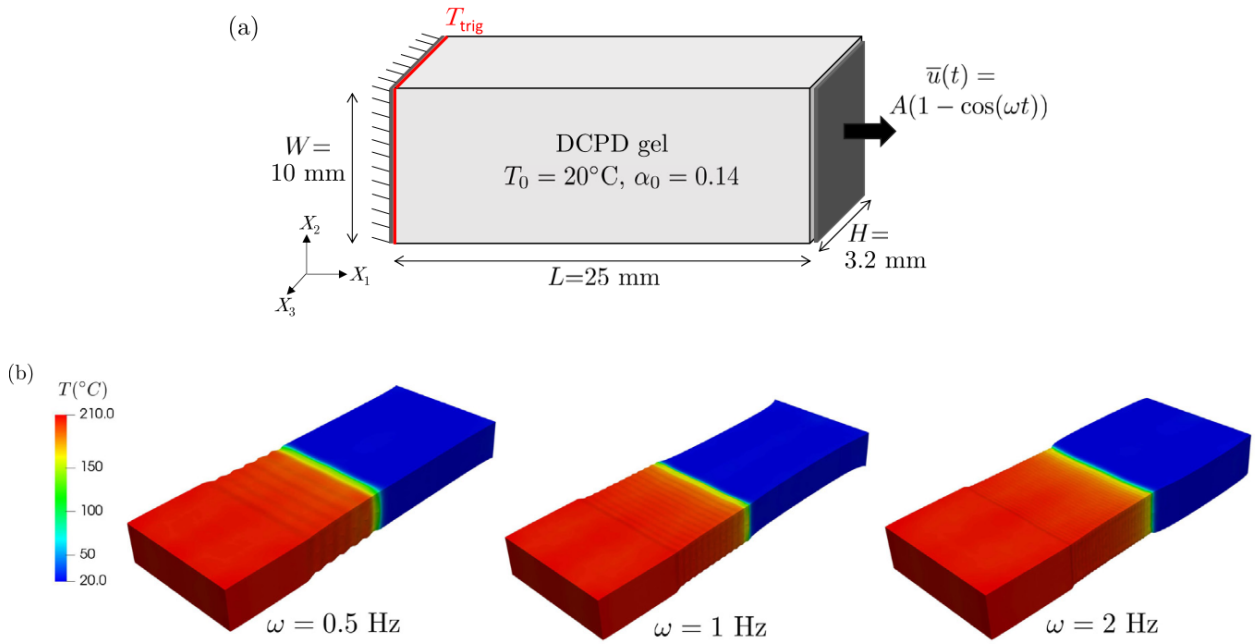

Fig. 11. Experiment on formation of periodic surface topography patterns through the application of uniaxial oscillatory load during linear propagation of a single front. (a) Schematic of the experimental geometry in its initial configuration at $t = 0$, and applied boundary and initial conditions. (b) Three-dimensional contour plots from the simulations of the temperature field in the deformed configuration at $t = 22.5$ s for three values of applied frequency $\omega = 0.5, 1, 2$ Hz.

Some samples were stored in a freezer (ca. −20°C) prior to testing, and it was determined that the degree of pre-cure and front velocity were not affected by freezer storage.

5.3. Application of loading during FP

Cyclic tensile loading was applied on DCPD gel specimen (3.2 mm thick, 10 mm wide, 25 mm gauge length) during FP using an Instron 8841 fatigue frame. The applied displacement amplitude was maintained at 2 mm for all experiments. Frequency was varied from 0.1–15 Hz. FP was initiated at one end of the gel using a hot soldering iron. The front velocity was determined from a linear fit of front position vs. time based on videos taken during FP. The true front velocity was not affected by the mechanical input confirming the numerical results in Section 4.1.

5.4. Characterization

Profilometry. Surface topography profiles were measured using a KLA-Tencor P-6 stylus profiler. Line scans were performed in the direction of linear front propagation. The data were post-processed via baseline correction to remove the effect of specimen waviness over long length scales. 3D optical profilometry was performed using a Keyence VHX-5000 digital microscope. Samples were spray-coated with thin layer of flat black paint prior to imaging.

Optical imaging. pDCPD specimens with surface topography patterns were imaged through a 5× or 10× objective using a Leica DMR optical microscope equipped with a QImaging Micropublisher camera. Specimens with large patterns with wavelength $\lambda > 1$ mm were imaged with an Epson scanner. Pattern wavelengths were measured in at least four locations of each specimen and then averaged. No difference was observed between measurements in different locations of the same specimen.

5.5. Experimental results and comparison with theory

Fig. 11(a) shows a schematic of the experiment. The initial degree of cure $\alpha_0 = 0.14$ corresponds to the samples for which the reaction fronts progresses at a constant velocity of 0.6 mm/s. The initial temperature of the gel is room temperature. The reaction front is allowed to initiate and propagate for $t = 10$ s from the left boundary of the domain before the oscillatory loading is initiated at the right boundary. The frequency of the applied oscillatory loading is varied over a range of $\omega = 0.1$ to 15 Hz. The corresponding simulations are conducted in 3-D with the same initial and boundary conditions for three values of applied frequency, $\omega = 0.5, 1, 2$ Hz. The material properties and initial conditions used in the simulations are summarized in Table 3.

Contour plots of the temperature field in the deformed configuration in 3-D at $t = 22.5$ s are shown in Fig. 11(b) for the three different values of frequency.

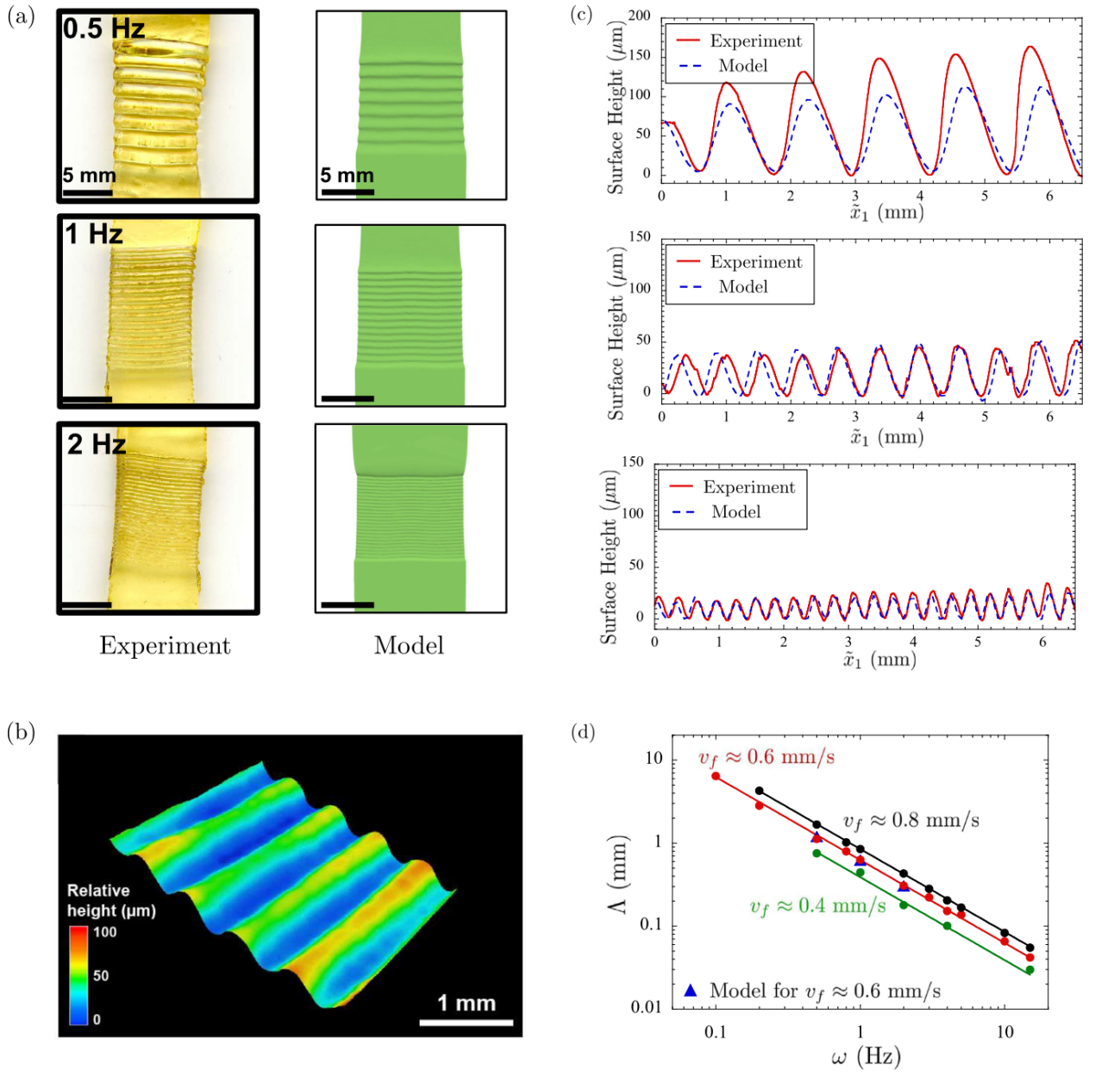

Fig. 12. Comparison of the proposed model with an experimental result for frontal polymerization under imposed cyclic loading with three values of constant frequency $\omega = 0.5, 1, 2$ Hz. (a) Surface patterns obtained experimentally (left column) and numerically (right column). (b) Experimental 3-D profile of a surface pattern produced for $\omega = 1$ Hz. (c) Relative height of the surface pattern in the x_3 direction along the direction of front propagation and in deformed coordinate $\tilde{x}_1 = x_1 - 7$ mm. (d) Pattern wavelength, Λ, as a function of imposed frequency, ω, for three sets of experiments with different front velocities (v_f) arising from different degrees of pre-cure (α_0). Model results are shown only for $v_f \approx 0.6$ mm/s.

Fig. 12 shows a direct comparison between the experimental and numerical results for the three values of frequency of applied load. In Fig. 12(a), we show images of the top surface of experimental specimens post-FP along with the corresponding images from the simulations. A representative 3-D surface profile of a periodic surface pattern from the experiments produced for $\omega =$ 1 Hz is shown in Fig. 12(b). In Fig. 12(c), we provide a quantitative comparison between the surface profiles obtained from the experiments and the simulations. We observe a fairly good agreement between the experimental and numerical results for all three imposed frequencies. The gap between the results for $\omega = 0.5$ Hz is potentially due to higher viscous effects at this frequency that have not been currently accounted for in the model. The strong dependence of the amplitude of the pattern on the imposed frequency is notable. Finally, in Fig. 12(d), we show a plot of pattern wavelength, Λ, as a function of imposed frequency, ω, for three sets of experiments with different values of α_0. These values of α_0 correspond to front velocity $v_f = 0.4, 0.6$ and 0.8 mm/s. We observe that the front velocity is unaffected by the value of imposed frequency and the pattern wavelength follows the relationship

$$\Lambda(\alpha_0) = \frac{v_f(\alpha_0)}{\omega} \tag{43}$$

Table 3
Summary of material parameters and initial conditions used in simulations.

Type	Property values	Source
Thermal	$\kappa = 0.15\,\mathrm{W/m\ K}$, $\rho_0 = 980\,\mathrm{kg/m^3}$, $C_p = 1600\,\mathrm{J/kg\ K}$, $\zeta = 10^{-4}\ \mathrm{K^{-1}}$	Vyas et al. (2019), Koohbor et al. (2022)
Cure kinetic	$A_a = 8.55 \times 10^{15}\,1/\mathrm{s}$, $E_a = 110,750\,\mathrm{J/mol}$, $n = 1.77$, $m = 0.81$, $c_d = 14.41$, $\alpha_d = 0.41$	Vyas et al. (2019)
Mechanical	$E_1 = 0.29\,\mathrm{MPa}$, $E_2 = 2100\,\mathrm{MPa}$, $\nu_1 = 0.4995$, $\nu_2 = 0.416$	Koohbor et al. (2022)
Elastic model (16)	$C = 20.30$, $\alpha_E = 0.79$, $D = 11.92$, $\alpha_\nu = 0.65$, $\alpha^h = 0.39$	Fitted to data from Koohbor et al. (2022)
Initial conditions	$T_0 = 20\ ^\circ\mathrm{C}$, $\alpha_0 = 0.14$	T_0 – room temperature, α_0 – corresponding to experimental front velocity 0.6 mm/s

as shown in the figure. Thus, we can tune the imposed frequency and the front velocity to reliably produce patterns of a desired wavelength over a range of more than two orders of magnitude, from 30 μm to 6 mm.

6. Conclusions

In this work, we have proposed a novel large deformation thermo-chemo-mechanical theory capable of describing the evolution of deformation and temperature fields during frontal polymerization of partially cured polymeric gels subjected to arbitrary quasi-static mechanical loads and thermal flux. The extensive analytical and numerical study conducted in Sections 3 and 4 demonstrate the capability of theory to respond to variety of mechanical and thermal input.

Furthermore, we have demonstrated pattern formation in pDCPD via the application of mechanical stress during FP of partially cured DCPD gels. This patterning technique was enabled by the directional nature of FP and the ability of the gels to withstand and respond to the input of mechanical force. Oscillatory mechanical inputs were imposed during FP of DCPD gels, leading to pDCPD specimens with periodic surface topography patterns. The pattern wavelength was controlled predictably by varying the frequency of the imposed mechanical input. We showed that the proposed theory is able to predict the experimental results well.

CRediT authorship contribution statement

Aditya Kumar: Conceptualization, Methodology, Software, Writing – original draft, Writing – review & editing. **Leon M. Dean:** Conceptualization, Methodology, Investigation, Writing – original draft. **Mostafa Yourdkhani:** Conceptualization, Methodology. **Allen Guo:** Investigation. **Cole BenVau:** Software. **Nancy R. Sottos:** Conceptualization, Methodology, Writing – review & editing, Supervision, Funding acquisition. **Philippe H. Geubelle:** Conceptualization, Methodology, Writing – review & editing, Supervision, Funding acquisition.

Declaration of competing interest

The authors declare that they have no known competing financial interests or personal relationships that could have appeared to influence the work reported in this paper.

Data availability

Data will be made available on request.

Acknowledgments

This work was part of a broader interdisciplinary effort to study frontal polymerization by the Autonomous Materials Systems (AMS) group at the Beckman Institute for Advanced Science and Technology. The authors gratefully acknowledge support from U. S. Air Force Office of Scientific Research through Award FA9550-20-1-0194 (Dr. B.“Les” Lee, Program Manager) as part of the Center for Excellence in Self-Healing, Regeneration, and Structural Remodeling. The authors also acknowledge the support of the National Science Foundation for Grant No. 1933932 through the GOALI: Manufacturing USA Program.

References

Ambrosi, D., Ateshian, G.A., Arruda, E.M., Cowin, S.C., Dumais, J., Goriely, A., Holzapfel, G.A., Humphrey, J.D., Kemkemer, R., Kuhl, E., Olberding, J.E., 2011. Perspectives on biological growth and remodeling. J. Mech. Phys. Solids 59 (4), 863–883.

Anand, L., 2012. A Cahn–Hilliard-type theory for species diffusion coupled with large elastic–plastic deformations. J. Mech. Phys. Solids 60 (12), 1983–2002.

Anguiano, M., Gajendran, H., Hall, R.B., Rajagopal, K.R., Masud, A., 2020. Chemo-mechanical coupling and material evolution in finitely deforming solids with advancing fronts of reactive fluids. Acta Mech. 231 (5), 1933–1961.

Anguiano, M., Masud, A., 2021. Reduced mixture model and elastic response of chemically swollen solids: Application to Si oxidation and lithiation. Appl. Eng. Sci. 6, 100039.

Aw, J.E., 2019. Simultaneous Three-Dimensional Printing and Frontal Polymerization of Dicyclopentadiene Resin (Masters thesis). University of Illinois at Urbana-Champaign.

Aw, J.E., Zhang, X., Nelson, A.Z., Dean, L.M., Yourdkhani, M., Ewoldt, R.H., Geubelle, P.H., Sottos, N.R., 2022. Self-regulative, free-form printing enabled by frontal polymerization. Adv. Mater. Technol. 2200230.

Bayly, P.V., Taber, L.A., Kroenke, C.D., 2014. Mechanical forces in cerebral cortical folding: a review of measurements and models. J. Mech. Behav. Biomed. Mater. 29, 568–581.

Bowden, G., Garbey, M., Ilyashenko, V.M., Pojman, J.A., Solovyov, S.E., Taik, A., Volpert, V.A., 1997. Effect of convection on a propagating front with a solid product: comparison of theory and experiments. J. Phys. Chem. B 101 (4), 678–686.

Cai, S., Suo, Z., 2011. Mechanics and chemical thermodynamics of phase transition in temperature-sensitive hydrogels. J. Mech. Phys. Solids 59 (11), 2259–2278.

Chechilo, N.M., Enikolopyan, N.S., 1974. Structure of the polymerization wave front and propagation mechanism of the polymerization reaction. Doklady Phys. Chem. 214 (5), 174–176.

Chechilo, N.M., Khvilivitskii, R.J., Enikolopyan, N.S., 1972. Propagation of the polymerization reaction. Dokl. Akad. Nauk SSSR 204, 1180–1181.

Cui, Z., Gao, F., Qu, J., 2012. A finite deformation stress-dependent chemical potential and its applications to lithium ion batteries. J. Mech. Phys. Solids 60 (7), 1280–1295.

Davtyan, S.P., Zhirkov, P.V., Vol'fson, S.A., 1984. Problems of non-isothermal character in polymerisation processes. Russ. Chem. Rev. 53 (2), 150.

Di Leo, C.V., Rejovitzky, E., Anand, L., 2015. Diffusion–deformation theory for amorphous silicon anodes: the role of plastic deformation on electrochemical performance. Int. J. Solids Struct. 67, 283–296.

Epstein, M., 2015. Mathematical characterization and identification of remodeling, growth, aging and morphogenesis. J. Mech. Phys. Solids 84, 72–84.

Epstein, M., Maugin, G.A., 2000. Thermomechanics of volumetric growth in uniform bodies. Int. J. Plast. 16 (7–8), 951–978.

Frulloni, E., Salinas, M.M., Torre, L., Mariani, A., Kenny, J.M., 2005. Numerical modeling and experimental study of the frontal polymerization of the diglycidyl ether of bisphenol A/diethylenetriamine epoxy system. J. Appl. Polym. Sci. 96 (5), 1756–1766.

Gao, X., Fang, D., Qu, J., 2015. A chemo-mechanics framework for elastic solids with surface stress. Proc. R. Soc. A Math. Phys. Eng. Sci. 471 (2182), 20150366.

Garbey, M., Taik, A., Volpert, V., 1996. Linear stability analysis of reaction fronts in liquids. Quart. Appl. Math. 54 (2), 225–247.

Gent, A.N., 1996. A new constitutive relation for rubber. Rubber Chem. Technol. 69 (1), 59–61.

Goldfeder, P.M., Volpert, V.A., Ilyashenko, V.M., Khan, A.M., Pojman, J.A., Solovyov, S.E., 1997. Mathematical modeling of free-radical polymerization fronts. J. Phys. Chem. B 101 (18), 3474–3482.

Goli, E., Peterson, S.R., Geubelle, P.H., 2020. Instabilities driven by frontal polymerization in thermosetting polymers and composites. Composites B 199, 108306.

Goli, E., Robertson, I.D., Geubelle, P.H., Moore, J.S., 2018. Frontal polymerization of dicyclopentadiene: a numerical study. J. Phys. Chem. B 122 (16), 4583–4591.

Haftbaradaran, H., Song, J., Curtin, W.A., Gao, H., 2011. Continuum and atomistic models of strongly coupled diffusion, stress, and solute concentration. J. Power Sources 196 (1), 361–370.

Ivanoff, D.G., Sung, J., Butikofer, S.M., Moore, J.S., Sottos, N.R., 2020. Cross-linking agents for enhanced performance of thermosets prepared via frontal ring-opening metathesis polymerization. Macromolecules 53 (19), 8360–8366.

Javadi, M., Epstein, M., Asghari, M., 2020. Thermomechanics of material growth and remodeling in uniform bodies based on the micromorphic theory. J. Mech. Phys. Solids 138, 103904.

Khanukaev, B.B., Kozhushner, M.A., Enikolopyan, N.S., Chechilo, N.M., 1974. Theory of the propagation of a polymerization front. Combust. Explos. Shock Waves 10 (1), 17–21.

Koohbor, B., Zhang, X., Dean, L.M., Yourdkhani, M., Geubelle, P.H., Sottos, N.R., 2022. Experimental characterization and multiphysics modeling of residual deformation in manufacturing of thermosetting polymers by frontal polymerization, (In preparation).

Kucken, M., Newell, A.C., 2005. Fingerprint formation. J. Theoret. Biol. 235 (1), 71–83.

Kuhl, E., 2014. Growing matter: a review of growth in living systems. J. Mech. Behav. Biomed. Mater. 29, 529–543.

Kumar, A., Francfort, G.A., Lopez-Pamies, O., 2018. Fracture and healing of elastomers: A phase-transition theory and numerical implementation. J. Mech. Phys. Solids 112, 523–551.

Kumar, A., Gao, Y., Geubelle, P.H., 2021. Analytical estimates of front velocity in the frontal polymerization of thermoset polymers and composites. J. Polym. Sci. 59 (11), 1109–1118.

Lopez-Pamies, O., 2010. A new I1-based hyperelastic model for rubber elastic materials. C. R. Méc. 338, 3–11.

Ma, S.J., Mannino, S.J., Wagner, N.J., Kloxin, C.J., 2013. Photodirected formation and control of wrinkles on a thiol–ene elastomer. ACS Macro Lett. 2 (6), 474–477.

Pojman, J.A., 1991. Traveling fronts of methacrylic acid polymerization. J. Am. Chem. Soc. 113 (16), 6284–6286.

Pojman, J.A., Craven, R., Khan, A., West, W., 1992. Convective instabilities in traveling fronts of addition polymerization. J. Phys. Chem. 96 (18), 7466–7472.

Pojman, J.A., Willis, J., Fortenberry, D., Ilyashenko, V., Khan, A.M., 1995. Factors affecting propagating fronts of addition polymerization: velocity, front curvature, temperatue profile, conversion, and molecular weight distribution. J. Polym. Sci. A Polym. Chem. 33 (4), 643–652.

Rejovitzky, E., Di Leo, C.V., Anand, L., 2015. A theory and a simulation capability for the growth of a solid electrolyte interphase layer at an anode particle in a Li-ion battery. J. Mech. Phys. Solids 78, 210–230.

Robertson, I.D., Dean, L.M., Rudebusch, G.E., Sottos, N.R., White, S.R., Moore, J.S., 2017. Alkyl phosphite inhibitors for frontal ring-opening metathesis polymerization greatly increase pot life. ACS Macro Lett. 6 (6), 609–612.

Robertson, I.D., Yourdkhani, M., Centellas, P.J., Aw, J.E., Ivanoff, D.G., Goli, E., Lloyd, E.M., Dean, L.M., Sottos, N.R., Geubelle, P.H., Moore, J.S., 2018. Rapid energy-efficient manufacturing of polymers and composites via frontal polymerization. Nature 557 (7704), 223–227.

Robling, A.G., Castillo, A.B., Turner, C.H., 2006. Biomechanical and molecular regulation of bone remodeling. Annu. Rev. Biomed. Eng. 8, 455–498.

Solovyov, S.E., Ilyashenko, V.M., Pojman, J.A., 1997. Numerical modeling of self-propagating polymerization fronts: The role of kinetics on front stability. Chaos 7 (2), 331–340.

Sozio, F., Yavari, A., 2019. Nonlinear mechanics of accretion. J. Nonlinear Sci. 29 (4), 1813–1863.

Ulm, F.J., Coussy, O., Kefei, L., Larive, C., 2000. Thermo-chemo-mechanics of ASR expansion in concrete structures. J. Eng. Mech. 126 (3), 233–242.

Van Essen, D.C., 1997. A tension-based theory of morphogenesis and compact wiring in the central nervous system. Nature 385 (6614), 313–318.

Volpert, V.A., Volpert, V.A., Pojman, J.A., Solovyov, S.E., 1996. Hydrodynamic stability of a polymerization front. European J. Appl. Math. 7 (3), 303–320.

Vyas, S., Goli, E., Zhang, X., Geubelle, P.H., 2019. Manufacturing of unidirectional glass-fiber-reinforced composites via frontal polymerization: A numerical study. Compos. Sci. Technol. 184, 107832.

Warden, S.J., Roosa, S.M.M., Kersh, M.E., Hurd, A.L., Fleisig, G.S., Pandy, M.G., Fuchs, R.K., 2014. Physical activity when young provides lifelong benefits to cortical bone size and strength in men. Proc. Natl. Acad. Sci. 111 (14), 5337–5342.

Weinkamer, R., Eberl, C., Fratzl, P., 2019. Mechanoregulation of bone remodeling and healing as inspiration for self-repair in materials. Biomimetics 4 (3), 46.

Yang, G., Lee, J.K., 2014. Curing kinetics and mechanical properties of endo-dicyclopentadiene synthesized using different Grubbs' catalysts. Ind. Eng. Chem. Res. 53 (8), 3001–3011.

Yourdkhani, M., Koohbor, B., Lamuta, C., Dean, L.M., Centellas, P., Ivanoff, D.G., Robertson, I.D., White, S.R., Sottos, N.R., 2019. Thermo-mechanical properties of thermoset polymers and composites fabricated by frontal polymerization. In: Mechanics of Composite, Hybrid and Multifunctional Materials, Vol. 5. Springer, Cham, pp. 89–91.